Climatology of Severe Local Storm Environments and Synoptic-Scale Features over North America in ERA5 Reanalysis and CAM6 Simulation

FUNING LI AND DANIEL R. CHAVAS

Department of Earth, Atmospheric, and Planetary Sciences, Purdue University, West Lafayette, Indiana

KEVIN A. REED

School of Marine and Atmospheric Sciences, Stony Brook University, State University of New York, Stony Brook, New York

DANIEL T. DAWSON II

Department of Earth, Atmospheric, and Planetary Sciences, Purdue University, West Lafayette, Indiana

(Manuscript received 23 December 2019, in final form 13 July 2020)

ABSTRACT

Severe local storm (SLS) activity is known to occur within specific thermodynamic and kinematic environments. These environments are commonly associated with key synoptic-scale features—including southerly Great Plains low-level jets, drylines, elevated mixed layers, and extratropical cyclones—that link the large-scale climate to SLS environments. This work analyzes spatiotemporal distributions of both extreme values of SLS environmental parameters and synoptic-scale features in the ERA5 reanalysis and in the Community Atmosphere Model, version 6 (CAM6), historical simulation during 1980–2014 over North America. Compared to radiosondes, ERA5 successfully reproduces SLS environments, with strong spatiotemporal correlations and low biases, especially over the Great Plains. Both ERA5 and CAM6 reproduce the climatology of SLS environments over the central United States as well as its strong seasonal and diurnal cycles. ERA5 and CAM6 also reproduce the climatological occurrence of the synoptic-scale features, with the distribution pattern similar to that of SLS environments. Compared to ERA5, CAM6 exhibits a high bias in convective available potential energy over the eastern United States primarily due to a high bias in surface moisture and, to a lesser extent, storm-relative helicity due to enhanced low-level winds. Composite analysis indicates consistent synoptic anomaly patterns favorable for significant SLS environments over much of the eastern half of the United States in both ERA5 and CAM6, though the pattern differs for the southeastern United States. Overall, our results indicate that both ERA5 and CAM6 are capable of reproducing SLS environments as well as the synoptic-scale features and transient events that generate them.

1. Introduction

Severe local storm (SLS) environments are favorable atmospheric conditions for the development of SLS events, including severe thunderstorms accompanied by damaging winds, large hailstones, and/or tornadoes (Ludlam 1963; Johns and Doswell 1992). Such environments are commonly defined by high values of a small number of key thermodynamic and kinematic parameters: convective available potential energy (CAPE), lower-tropospheric (0–6-km) bulk vertical wind shear (S06), and 0–3-km storm-relative helicity (SRH03) (Rasmussen and Blanchard 1998; Rasmussen 2003; Brooks et al. 2003; Doswell and Schultz 2006; Grams et al. 2012). CAPE is the vertical integral of buoyancy from the level of free convection to the equilibrium level and thus provides a measure of conditional instability for a potential storm (Doswell and Rasmussen 1994). Given the standard assumptions of parcel theory, CAPE is proportional to the theoretical maximum updraft wind speed (Holton 1973). S06 and SRH03 are proxies of environmental crosswise and streamwise vorticity available to generate updraft rotation (Rotunno and Klemp 1982, 1985; Davies-Jones et al. 1990; Davies-Jones 1993; Weisman and Rotunno 2000;

Supplemental information related to this paper is available at the Journals Online website: https://doi.org/10.1175/JCLI-D-19-0986.s1.

Corresponding author: Funing Li, li3226@purdue.edu

DOI: 10.1175/JCLI-D-19-0986.1

Davies-Jones 2002; Rotunno and Weisman 2003; Davies-Jones 2003). These conditions work in combination to permit the generation of persistent rotating updrafts that are the defining characteristic of supercell storms (Doswell and Burgess 1993). Given that both thermodynamic and kinematic "ingredients" are necessary, composite proxies, such as the product of CAPE and S06 (CAPES06) and the energy helicity index (EHI03; proportional to the product of CAPE and SRH03), are commonly employed as representative measures of the SLS potential of a given environment (Davies-Jones 1993; Brooks et al. 2003; Thompson et al. 2003). In general, composite proxies are preferable to the constituent parameters alone in discriminating conducive environments for SLS events (Rasmussen and Blanchard 1998; Brooks et al. 2003), while the individual constituent parameters are indicative of the key underlying physical processes (Doswell and Schultz 2006).

The generation of SLS environments over the Great Plains of North America is intimately associated with key synoptic-scale features, including the southerly Great Plains low-level jets (GPLLJs), drylines, elevated mixed layers (EMLs), and extratropical cyclones. Southerly GPLLJs, defined by a local maximum in low-level winds, commonly form during the nighttime (Bonner 1968; Whiteman et al. 1997). GPLLJs modulate Great Plains precipitation (Weaver and Nigam 2008) and its moisture budget by transporting almost one-third of the moisture that enters the contiguous United States (Helfand and Schubert 1995), which is an important contributor to the formation of high-CAPE environments (Helfand and Schubert 1995; Higgins et al. 1997; Weaver et al. 2012). Drylines and EMLs are associated with the eastward advection of well-mixed air with relatively high potential temperature generated by strong surface heating over the elevated dry deserts of the Mexican Plateau. Meridionally oriented drylines are common across the central and southern Great Plains when this dry airmass from the west encounters the moist near-surface air mass advected northward from the Gulf of Mexico (Fujita 1958; Schaefer 1974; Ziegler and Hane 1993; Hoch and Markowski 2005), producing a focused linear band of convergence and moisture gradients (Rhea 1966; Ziegler and Rasmussen 1998; Xue and Martin 2006; Schultz et al. 2007). The advection of the well-mixed layer atop the low-level moist air generates the EML, often creating a strong capping inversion at the base of the EML (Carlson et al. 1983; Lanicci and Warner 1991a; Banacos and Ekster 2010). Subsequent daytime heating of the moist boundary layer allows for the gradual removal of convective inhibition and buildup of CAPE (Carlson et al. 1983; Farrell and Carlson 1989; Lanicci and Warner 1991b,c; Cordeira et al. 2017). Extratropical cyclones strongly enhance low-level moisture and heat convergence within their warm sectors, thereby enhancing CAPE (Hamill et al. 2005; Tochimoto and Niino 2016). Moreover, the cyclonic circulation itself, as well as baroclinic instability that drives extratropical cyclone evolution, also act to enhance the vertical wind shear (Doswell and Bosart 2001).

Previous studies have documented the climatological variability, including the amplitude and spatial pattern, of the SLS environmental proxies and parameters (Brooks et al. 2003; Wagner et al. 2008; Gensini and Ashley 2011; Diffenbaugh et al. 2013; Tippett et al. 2015; Gensini and Brooks 2018; Gensini and Bravo de Guenni 2019; Tang et al. 2019), as well as the key synoptic-scale features that help generate these environments (Bonner 1968; Reitan 1974; Zishka and Smith 1980; Lanicci and Warner 1991a; Whiteman et al. 1997; Hoch and Markowski 2005; Duell and Van Den Broeke 2016; Ribeiro and Bosart 2018). It is known from these studies that SLS environments and associated synoptic-scale features have strong seasonal and diurnal cycles, which indicates the important role of two fundamental types of external climate forcing (solar insolation variation due to Earth's rotation and tilt) in driving potential SLS activity. However, these studies have analyzed different geographic domains and time periods using different datasets, which makes holistic analysis and intercomparison difficult.

Reanalysis datasets, combining multisource observations and model-based forecasts via advanced data assimilation methods, provide a synthesized representation of the atmosphere over long historical time periods and thus have become an indispensable data source for the study of weather and climate from synoptic to planetary scales. Several reanalysis datasets have been used to investigate the climatological distribution or variation of SLS environments, including NCEP–NCAR (Brooks et al. 2003; Diffenbaugh et al. 2013), North American Regional Reanalysis (NARR; Gensini and Ashley 2011; Gensini et al. 2014a; Tippett et al. 2016; Gensini and Brooks 2018; Tang et al. 2019), and ERA-Interim (Allen and Karoly 2014; Taszarek et al. 2018). These reanalysis datasets in general produce similar spatial patterns but slightly different magnitudes for the climatology of SLS environments. Recent work evaluated the performance of ERA-Interim and NARR in estimating the environmental proxies and parameters by comparing them with radiosonde measurements (Gensini et al. 2014a; Taszarek et al. 2018), indicating that these reanalysis datasets reproduce the observed spatiotemporal trends of SLS environments, though they exhibit larger regional biases in thermodynamic parameters (e.g., CAPE) than in kinematic parameters (e.g., S06). In addition, these reanalysis datasets in general produce lower biases over flat terrain

than in coastal areas and mountains owing to the limited horizontal resolution and sharp variations of atmospheric variables across regions with complex topography (Taszarek et al. 2018). Hence, a higher-resolution reanalysis dataset is expected to better represent these environments. Overall, caution is needed when interpreting results from reanalysis datasets considering the varying uncertainties associated with the representation of the surface and atmosphere and data assimilation schemes (Parker 2016). Ultimately, evaluation of a reanalysis dataset is necessary to identify its potential strengths and limitations for studying SLS environments (Gensini et al. 2014a).

Additionally, global climate models have been a useful tool to study SLS environments (Tippett et al. 2015). As with reanalysis datasets, such models lack sufficient horizontal resolution to resolve actual SLS events, but they are capable of resolving larger-scale SLS environments. Though climate models do not reproduce the true historical day-to-day weather, they are able to capture the statistical behavior of the present-day climate. Thus, climate models have been widely used to analyze SLS environments in current or future climate simulations to assess the impacts of climate changes on SLS activity, assuming that changes in SLS activity will follow changes in the statistics of SLS environments (Trapp et al. 2007; Diffenbaugh et al. 2013; Romps et al. 2014; Seeley and Romps 2015; Tippett et al. 2016; Gensini and Brooks 2018). These models in general reproduce a reasonable historical climatology of SLS environments, though biases vary across models when compared to the reanalysis- or radiosonde-based climatology (Diffenbaugh et al. 2013; Seeley and Romps 2015). Forced with coarse-resolution output from global climate models, dynamical downscaling through high-resolution regional climate models has shown substantial potential for assessment of both SLS events and environments (Trapp et al. 2011; Robinson et al. 2013; Gensini and Mote 2014, 2015; Hoogewind et al. 2017).

The purpose of this study is therefore to evaluate the representations of both SLS environments and synoptic-scale features commonly associated with the generation of these environments over North America in a new high-resolution global reanalysis dataset, which is the fifth major global reanalysis produced by ECMWF (ERA5), and a global climate model [Community Atmosphere Model, version 6 (CAM6)]. A comprehensive analysis and comparison of the climatologies of these environments and the synoptic-scale features provides an important reference for using reanalysis datasets and climate models to better understand climate controls on SLS activities in any climate state.

This work addresses the following questions:

1) How well does the ERA5 reanalysis represent the observed climatology of SLS environments over the contiguous United States?
2) How does this climatology, including seasonal and diurnal cycles, compare between the ERA5 reanalysis and CAM6 simulation?
3) What are the climatological distributions of the key synoptic-scale features commonly associated with the generation of SLS environments over North America in the ERA5 reanalysis and CAM6 simulation?
4) What are the characteristic synoptic patterns associated with SLS environments in the ERA5 reanalysis and CAM6 simulation? Do they vary from region to region?

To answer these questions, we first compare SLS environments between ERA5 and radiosondes. This examines the ability of ERA5 to reproduce both the statistical properties of the present-day SLS climate and the observed day-to-day weather variability in SLS environments. As climate models simulate climate statistics but not observed day-to-day weather, we then compare the climatology, including seasonal and diurnal cycles, of SLS environments and the associated synoptic-scale features between ERA5 and the CAM6 simulation and analyze biases in CAM6. Finally, we create and compare synoptic composites associated with extreme SLS environments within a set of predefined regions across the eastern half of the United States to evaluate the extent to which CAM6 reproduces the characteristic synoptic-scale flow patterns that generate these events across regions.

Section 2 introduces the data, experimental design, and our analysis methodology. Section 3 evaluates ERA5 representations of SLS environments against radiosonde observations. Section 4 analyzes climatologies of SLS environments and the associated synoptic-scale features, and synoptic composites in ERA5 and CAM6. Finally, section 5 summarizes key conclusions and discusses avenues for future work.

2. Methodology

a. Datasets

We use radiosonde observations for the period 1998–2014, and the ERA5 reanalysis and CAM6 historical simulation data each for the period 1980–2014. The radiosondes are first used to evaluate the representation of SLS environments in ERA5 over the contiguous United States. The CAM6 simulation is then compared in-depth to ERA5 for North America. Each data source is described in detail below.

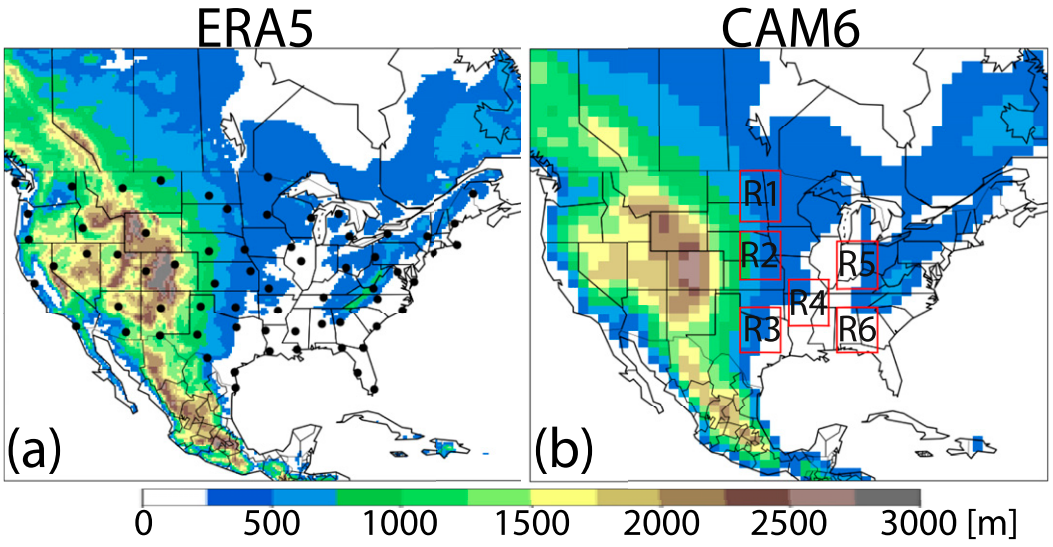

FIG. 1. Elevation map for (a) ERA5 reanalysis and (b) CAM6 simulation over North America. Black dots indicate locations of the 66 radiosonde stations over the contiguous United States. Labels R1–R6 denote the six 5° × 5° subregion boxes selected for regional analysis.

1) OBSERVATIONS: RADIOSONDE

Radiosonde observations are obtained from the sounding database of the University of Wyoming (http://weather.uwyo.edu/upperair/sounding.html). This dataset includes 69 radiosonde stations over the contiguous United States with twice-daily raw soundings at 0000 and 1200 UTC. Three stations (the KUNR station over western South Dakota, the KVEF station over southern Nevada, and the KEYW station on the island of Key West) are excluded in this study because of a lack of multiyear records, resulting in 66 stations (Fig. 1a). Roughly half of the radiosonde stations from the database do not have records before 1994 and most stations were moved 0.01°–0.03° longitude or latitude in 1990s (in or before 1997) due to the National Weather Service modernization. Thus, we only use radiosonde observations for the period 1998–2014 in this work, similar to Gensini et al. (2014a). Furthermore, we apply the following quality-control checks to each sounding before use: 1) height and pressure arrays are in correct order: height increases and pressure decreases with time; 2) wind speed ≥ 0 kt (1 kt $\approx 0.51\,\mathrm{m\,s^{-1}}$), $0° \leq$ wind direction $\leq 360°$, and temperature and dewpoint temperature ≥ 0 K; 3) height of the first record equals the local elevation; 4) top height > 6 km and top pressure < 100 hPa; and 5) the maximum pressure decrease between consecutive records ≤ 50 hPa. The first two checks follow the quality control done in SHARPpy (Blumberg et al. 2017); the third check ensures that the ground surface observation is available for calculating the surface-based CAPE; the fourth and fifth checks ensure that the vertical resolution of the sounding is identical with or higher than ERA5, as the purpose of using radiosondes is to evaluate ERA5 representations. The number percentage of qualified records for each radiosonde station is over 60% (Fig. S1a in the supplemental material).

2) REANALYSIS: ERA5

ERA5 spans the period 1979–present (Hersbach and Dee 2016). Here we use years 1980–2014, downloaded from NCAR's Research Data Archive (ECMWF 2019), for direct comparison with radiosondes and climate model simulation (described below). The dataset provides hourly variables at or near the surface and 37 constant pressure levels from 1000 to 1 hPa. These pressure-level data are produced by interpolating from the ECMWF's Integrated Forecast System with 137 hybrid sigma-pressure model levels in the vertical that extend up to a top level of 0.01 hPa (Hersbach and Dee 2016); this reduction of vertical resolution may induce small errors in calculations of vertically integrated parameters, such as CAPE and SRH03 (defined below). The horizontal grid spacing of ERA5 is 0.25° (roughly 31 km), which is higher than its predecessor ERA-Interim (79 km; Dee et al. 2011). Other improvements in ERA5 include using a revised data assimilation system and improved core dynamics and model physics (Hersbach and Dee 2016).

3) MODELING: CAM6

CAM6 is used for the simulation portion of this work. CAM6 is the atmospheric component of the Community Earth System Model, version 2.1 (available at http://

www.cesm.ucar.edu/models/cesm2/) developed in part for participation in phase6 of the Coupled Model Intercomparison Project (CMIP6; Eyring et al. 2016). CAM6 builds off its predecessor CAM5 (documented in detail in Neale et al. 2012) with significant modifications to the physical parameterization suite. In particular, CAM5 schemes for cloud macrophysics, boundary layer turbulence and shallow convection have been replaced by the Cloud Layers Unified by Binormals (CLUBB; Golaz et al. 2002; Bogenschutz et al. 2013) scheme. In addition, CAM6 now implements the two-moment prognostic cloud microphysics scheme from Gettelman and Morrison (2015), as well as additional updates to the Zhang and McFarlane (1995) deep convection and orographic drag parameterizations. CAM6 is configured with the default finite volume dynamical core on a 0.9° × 1.25° latitude–longitude grid mesh with 32 hybrid sigma-pressure levels. Our CAM6 simulation is configured as a historical simulation following the Atmospheric Model Intercomparison protocols (AMIP; Gates et al. 1999) over the period 1979–2014. We discard the first year for spinup and analyze the 3-hourly output from 1980 to 2014 for direct comparison with ERA5.

b. Analysis

We perform a climatological analysis of: 1) the annual, seasonal, and diurnal distributions of extreme SLS environmental proxies and their constituent parameters (defined below) over North America; 2) the occurrence frequency distributions of key synoptic-scale features including southerly Great Plains low-level jets, drylines, elevated mixed layers, and extratropical cyclone activity over North America; and 3) characteristic synoptic composites associated with extreme SLS environments in different geographic regions over the eastern half of the United States. To evaluate ERA5 performance using radiosondes, we extract ERA5 at 0000 and 1200 UTC for 1998–2014, consistent with the radiosonde temporal resolution and coverage, and then linearly interpolate the ERA5 results onto the radiosonde sites. To compare simulation with reanalysis, calculations for ERA5 and CAM6 are all done for 3-hourly outputs from 1980 to 2014 and then linearly interpolated onto 1° × 1° grids using the function "matplotlib.mlab.griddata" in the open-source matplotlib Python package (Hunter 2007).

1) SLS ENVIRONMENTS

(i) SLS environmental proxies and parameters

We calculate two combined proxies, CAPES06 and EHI03, to represent SLS environments. CAPES06 (Brooks et al. 2003) and EHI03 (Hart and Korotky 1991; Davies-Jones 1993) are calculated by

$$\mathrm{CAPES06} = \mathrm{CAPE} \times \mathrm{S06}, \tag{1}$$

and

$$\mathrm{EHI03} = \frac{\mathrm{CAPE} \times \mathrm{SRH03}}{160\,000\ \mathrm{m^4\,s^{-4}}}, \tag{2}$$

respectively. As for each constituent parameter, CAPE is defined as (Doswell and Rasmussen 1994):

$$\mathrm{CAPE} = \int_{z_{\mathrm{LFC}}}^{z_{\mathrm{EL}}} g\frac{T_{vp} - T_{ve}}{T_{ve}}\,dz, \tag{3}$$

where $g = 9.81\ \mathrm{m\,s^{-2}}$ is the acceleration due to gravity; z_{LFC} denotes the level of free convection, z_{EL} denotes the equilibrium level; and T_{vp} and T_{ve} are the virtual temperature of the 2-m parcel and the environment, respectively. Here we select the 2-m parcel for simplicity and its consistent availability across all our datasets; it also avoids biases in defining other types of parcels (e.g., most-unstable or mixed-layer parcel) associated with differences in the vertical resolutions of the datasets. S06 is defined as the magnitude of difference of wind vectors at 6 km ($\mathbf{V}_{6\mathrm{km}}$) and 10 m ($\mathbf{V}_{10\mathrm{m}}$) above the surface (Rasmussen and Blanchard 1998; Weisman and Rotunno 2000):

$$\mathrm{S06} = |\mathbf{V}_{6\mathrm{km}} - \mathbf{V}_{10\mathrm{m}}|. \tag{4}$$

SRH03 is defined as (Davies-Jones et al. 1990)

$$\mathrm{SRH03} = -\int_{z_b}^{z_t} \mathbf{k} \cdot (\mathbf{V} - \mathbf{C}) \times \frac{\partial \mathbf{V}}{\partial z}\,dz, \tag{5}$$

where $\mathbf{V}$ is horizontal wind vector, $\mathbf{C}$ is the storm motion vector following the definition and calculation from Bunkers et al. (2000), $z_b = 10$ m is the altitude of the layer bottom, $z_t = 3$ km is the altitude of the layer top, and $\mathbf{k}$ is the vertical unit vector. All variables needed for calculating these parameters are directly provided by each dataset except: 1) the 10-m wind direction in CAM6 (wind speed is provided), which we assume to be the same as the lowest model level; and 2) the 2-m mixing ratio in ERA5, which we calculate from the 2-m dewpoint temperature using Eq. (7.4) from Part IV in the documentation of the ECMWF IFS for CY41R2 (https://www.ecmwf.int/node/16648). Finally, we calculate climatologies of SLS environments using CAPES06 and EHI03, respectively, as well as their constituent parameters (CAPE, S06, and SRH03).

(ii) Analysis of extremes

We define SLS environments using the 99th percentile of the proxies and parameters, similar to past work (Tippett et al. 2016; Singh et al. 2017). The 99th percentile is calculated at each station site (for radiosondes)

or each grid point (for ERA5 or CAM6) based on the full-period (1998–2014 or 1980–2014) time series of each proxy or parameter at a given location. We also analyzed the 95th, 90th, and 75th percentiles, and found qualitatively similar climatological patterns across these high percentiles (detailed below in section 4a).

2) SLS-RELEVANT SYNOPTIC-SCALE FEATURES

(i) Southerly Great Plains low-level jet (GPLLJ)

We follow Bonner (1968) and Whiteman et al. (1997) to identify low-level jets (LLJs). The method detects LLJs and defines an intensity category 0–3 based on two criteria: 1) the maximum wind speed below 3000 m: $V_{max} \geq 10$, 12, 16, or 20 m s^{-1} and 2) the largest decrease from V_{max} in the layer from the height of V_{max} to 3000 m: $\Delta V \geq 5$, 6, 8, or 10 m s^{-1}. To identify specifically southerly LLJs, each detected LLJ is further classified as southerly if the direction of V_{max} falls between 113° and 247°, and as northerly if between 293° and 67° following Walters et al. (2008) and Doubler et al. (2015). Using these category- and direction-based criteria, we successfully detect various LLJs over North America, including the southerly and northerly GPLLJ, the northerly Pacific coast LLJ, the northerly Tehuantepec LLJ, and the easterly Caribbean LLJ, as documented in Doubler et al. (2015). The climatology of southerly GPLLJ in category 0 ($V_{max} \geq 10$ m s^{-1} and $\Delta V \geq 5$ m s^{-1}) is presented in this work.

(ii) Dryline

Drylines are identified at each grid point following the criteria in Duell and Van Den Broeke (2016): 1) the horizontal gradient of the surface specific humidity is at least 0.03 g kg^{-1} km^{-1} and the specific humidity gradient from west to east must be positive, 2) the surface temperature gradient from west to east is less than 0.02 K km^{-1}, and 3) a surface wind shift exists with wind direction on the west side between 170° and 280°, and on the east side between 80° and 190°. The first criterion is consistent with the approach of Hoch and Markowski (2005), in which the specific humidity gradient is preferable to the dewpoint temperature gradient, as the specific humidity is less sensitive to varying elevation. The other two criteria are used to differentiate drylines from cold fronts. The limitations of the algorithm are further discussed in Duell and Van Den Broeke (2016).

(iii) Elevated mixed layer (EML)

An EML is identified for a sounding that satisfies the following criteria, based on Banacos and Ekster (2010) and Ribeiro and Bosart (2018): 1) a candidate EML is identified as a layer with lapse rate equal to or greater than 8.0 K km^{-1} through a depth of at least 200 hPa, 2) the environmental relative humidity increases from the base to the top of the candidate EML, 3) the base of the candidate EML is at least 1000 m above the surface but below the 500-hPa level, and 4) the average lapse rate between the base and the surface is less than 8.0 K km^{-1}. Here, the EML base is defined as the first model level from the bottom with lapse rate equal to or greater than 8.0 K km^{-1}. The third and fourth criteria ensure the exclusion of surface-based or upper-tropospheric mixed layers.

(iv) Extratropical cyclone activity

Extratropical cyclone activity is defined using two methods: 1) cyclone track frequency calculated from explicit tracking of cyclone centers, and 2) eddy kinetic energy (EKE), which captures the spatial distribution of eddy activity in general.

The open-source TempestExtremes tracking algorithm (Ullrich and Zarzycki 2017) is used to detect and track individual extratropical cyclones using similar criteria described in Zarzycki (2018). Candidate cyclones are determined by searching for minima in sea level pressure with a closed contour of 2 hPa within 6 great circle degrees of the minimum. Candidate cyclones, which are detected at 3-hourly increments, are then stitched together in time by searching within an 8° great circle radius at the next time increment for another candidate cyclone to form a cyclone track. For a cyclone track to be included in the analysis it must exist for at least 9 time slices representing a minimum cyclone track length of 24 h.

EKE at 850 hPa is calculated by

$$\mathrm{EKE} = \frac{1}{2}(u'^2 + v'^2), \tag{6}$$

where $(u', v') = (u - \overline{u}, v - \overline{v})$ represent zonal and meridional velocity deviations from the annual mean velocities $(\overline{u}, \overline{v})$, the latter obtained by averaging the velocities (u, v) over the entire study period (1980–2014). Calculating (u', v') with respect to a multiyear, annual, or moving seasonal average does not change the amplitude or phase of the seasonal cycle of EKE significantly (Rieck et al. 2015). Following past work (Blackmon 1976; Ulbrich et al. 2008; Harvey et al. 2014; Schemm and Schneider 2018), we apply a 2–6-day Butterworth bandpass filter (Russell 2006) to (u', v') to retain reasonable time scales of extratropical cyclone activities before calculating EKE using Eq. (6). Other bandpass ranges, such as 2–8-day (Yin 2005) and 3–10-day (Kaspi and Schneider 2013; Tamarin and Kaspi 2016), are also tested. EKE is quantitatively sensitive to the bandpass range: longer range (e.g., 2–8-day versus 2–6-day) translates to larger EKE, but the qualitative

spatial pattern and seasonal variation of EKE are not sensitive to these ranges (not shown).

3) SYNOPTIC COMPOSITES FOR EXTREME CASES

We calculate the composite of synoptic anomalies conditioned on extreme SLS environments within six 5° ×5° regions (i.e., R1–R6 in Fig. 1b) from ERA5 and CAM6. R2–R4 are selected following Ribeiro and Bosart (2018); we also select subregions over the northern Great Plains (R1), the Midwest (R5), and the southeastern United States (R6), so that our analysis spans much of the land east of the Rocky Mountains where SLS activity and environments are concentrated. In this study, we define an extreme case in a region when the CAPES06 exceeds its local 99th percentile (i.e., within the top 1%) in at least 80% of the total grid points within the region. To generate the composite synoptic anomalies for each region, we first calculate the synoptic anomalies of each case from the full-period (1980–2014) monthly mean state (e.g., for a case selected in July 2012, the anomaly field of a variable is the difference between the variable field from the case and the mean field of the variable during 1980–2014 in July). Then, we generate composite synoptic anomalies at 250 hPa (horizontal winds and geopotential height), 700 hPa (horizontal winds, temperature, and geopotential height), and the surface (10-m winds, 2-m specific humidity, and sea level pressure) by averaging the anomaly fields of the extreme cases for each region. The composite synoptic patterns based on a 50% gridpoint coverage threshold is qualitatively similar, though with less distinctive features (e.g., a smoothed trough or wind fields; not shown). The 50% threshold produces more candidates for each region than the 80% threshold does, but also introduces larger variance that may reduce similarity across cases.

3. Results: Radiosonde and ERA5

We begin by comparing the extreme values (99th percentile) of SLS environmental parameters and proxies in the ERA5 reanalysis against radiosondes to investigate the extent to which ERA5 can reproduce the observed SLS environments. We first calculate the pattern correlation coefficient between ERA5 and radiosondes, as well as the bias (defined as percentage difference from radiosonde value) in ERA5 for each parameter and proxy (Fig. 2). ERA5 in general performs well in reproducing extreme values of these constituent parameters, with strong pattern correlation (CAPE: 0.93; S06: 0.93; SRH03: 0.83; Figs. 2a–c) and relatively low bias, especially over the Great Plains (~ ±10%; Figs. 2f–h). Specifically, extreme CAPE is generally underestimated (from −10% to 0% for the central Great Plains; from −40% to −10% for other areas) for most stations east of the Rocky Mountains and overestimated (~40%) over high terrains to the west (Fig. 2f); extreme S06 has the smallest bias (within ±10%) across most stations (Fig. 2g); extreme SRH03 is generally underestimated over central and western United States with relatively low bias over the Great Plains (within ±10%), while overestimated over eastern United States (10%–40%; Fig. 2h). Owing to the strong pattern correlations in these constituent parameters, the combined proxies, CAPES06 and EHI03, also have strong pattern correlations (CAPES06: 0.91; EHI03: 0.95), though they are in general underestimated by ERA5 (Figs. 2d,e). Biases of extreme CAPES06 is similar to the biases of extreme CAPE; biases of extreme EHI03 are slightly enhanced due to the combined influence of the constituent parameters, with negative bias of generally from −40% to −10% across most stations over the central United States and from −80% to −40% over western and northeastern United States (Figs. 2i,j).

Similar good performance is found for the full-period (1998–2014) time series of each parameter and proxy at each station in terms of the temporal correlation (Figs. 3a–e) and root-mean-square error (RMSE; Figs. 3f–j). Here we condition the radiosondes on CAPE ≥ 500 J kg^{-1}, as our focus is on the environments that could support SLS events. This threshold is only applied to CAPE (and thus CAPES06 and EHI03), resulting in a smaller sample size at each site for these parameters (Fig. S1c) than for S06 and SRH03 (Fig. S1a). ERA5 has relatively strong temporal correlations (~0.8) and small RMSEs (~40%) for CAPE over the Great Plains and the Midwest as compared to other areas (Figs. 3a,f), and does an excellent job in representing S06 at all sites (temporal correlation > 0.8; RMSE < 20%; Figs. 3b,g) and SRH03 over eastern half of the United States (temporal correlation > 0.8; 40% < RMSE < 60%; Figs. 3c,h). Regarding CAPES06 (Figs. 3d,i) and EHI03 (Figs. 3e,j), stations over the Great Plains in general have strong temporal correlation (>0.8) and relatively low RMSE (CAPES06: 40%–60%; EHI03: 60%–80%) as compared to the western United States and eastern coastal areas. Additionally, we perform similar analyses but condition CAPE, CAPES06, and EHI03 on CAPE ≥ 0 J kg^{-1}, as SLS events also occur within low-CAPE environments (e.g., the SLS activity commonly associated with low-CAPE, high-shear environments over the Southeast). By including these low-CAPE cases, both the temporal correlations and RMSEs of CAPE, CAPES06, and EHI03 increase (Fig. S2), indicating persistent and relatively large biases for the low-CAPE cases. Note though that including cases with CAPE below 500 J kg^{-1} skews the majority of our dataset to these relatively low CAPE values and so is much less representative of significant SLS environments.

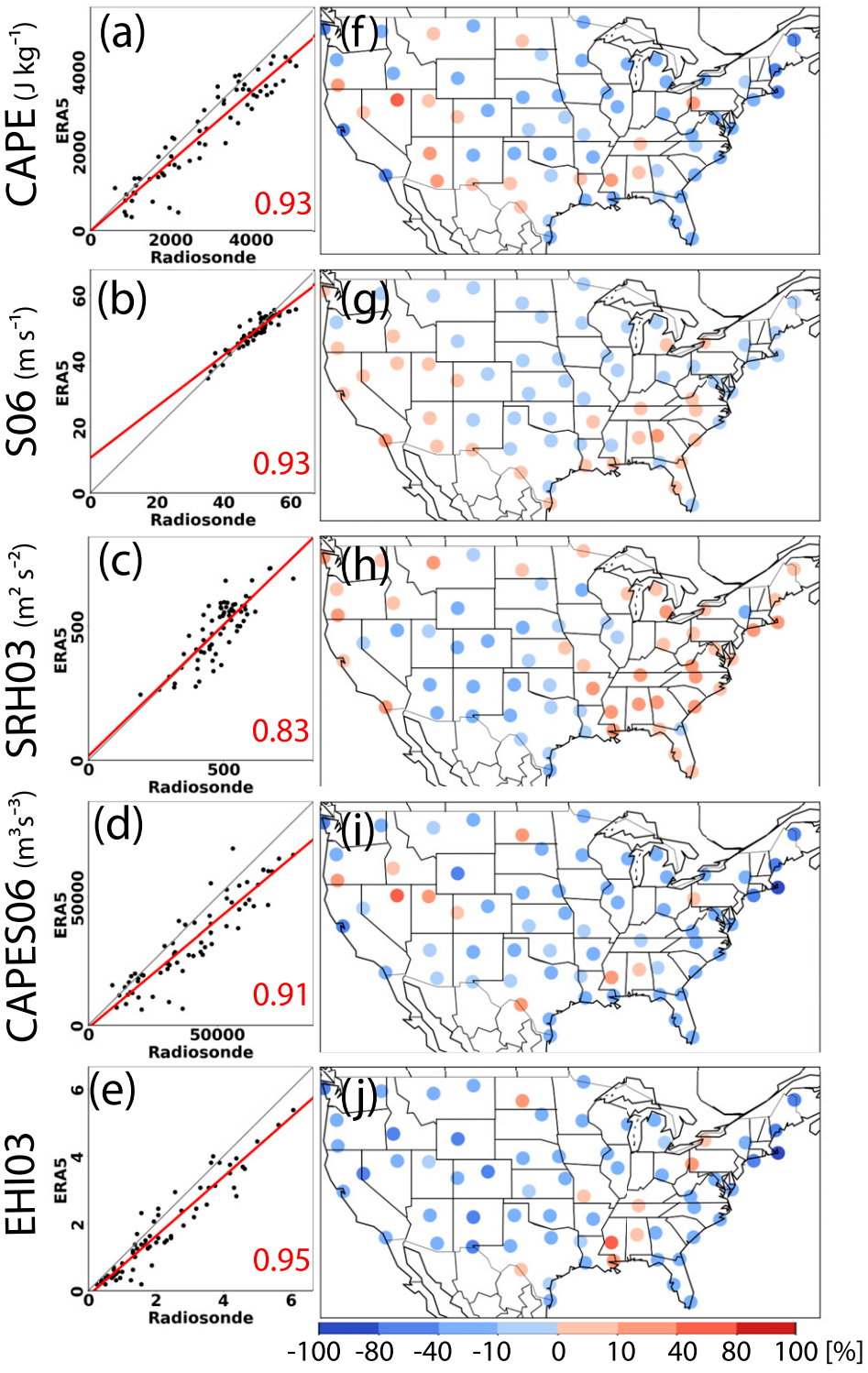

FIG. 2. ERA5 reanalysis vs radiosonde observations for the 99th percentiles of (from top to bottom) CAPE, S06, SRH03, CAPES06, and EHI03. (a)–(e) Scatterplot (black dots) of the 99th percentile values from ERA5 and radiosondes at each site (66 sites in total) with linear least squares fit (red line) and pattern correlation coefficient (red text); gray line denotes a one-to-one fit. (f)–(j) Bias of ERA5 99th percentile for each site, defined as percentage difference (ERA5 minus radiosondes). The 99th percentiles are generated from 0000 to 1200 UTC data during 1998–2014 for each site. The sample size from radiosondes at each site is shown in Fig. S1a. ERA5 99th percentiles are first generated at ERA5 grids and then linearly interpolated onto radiosonde sites.

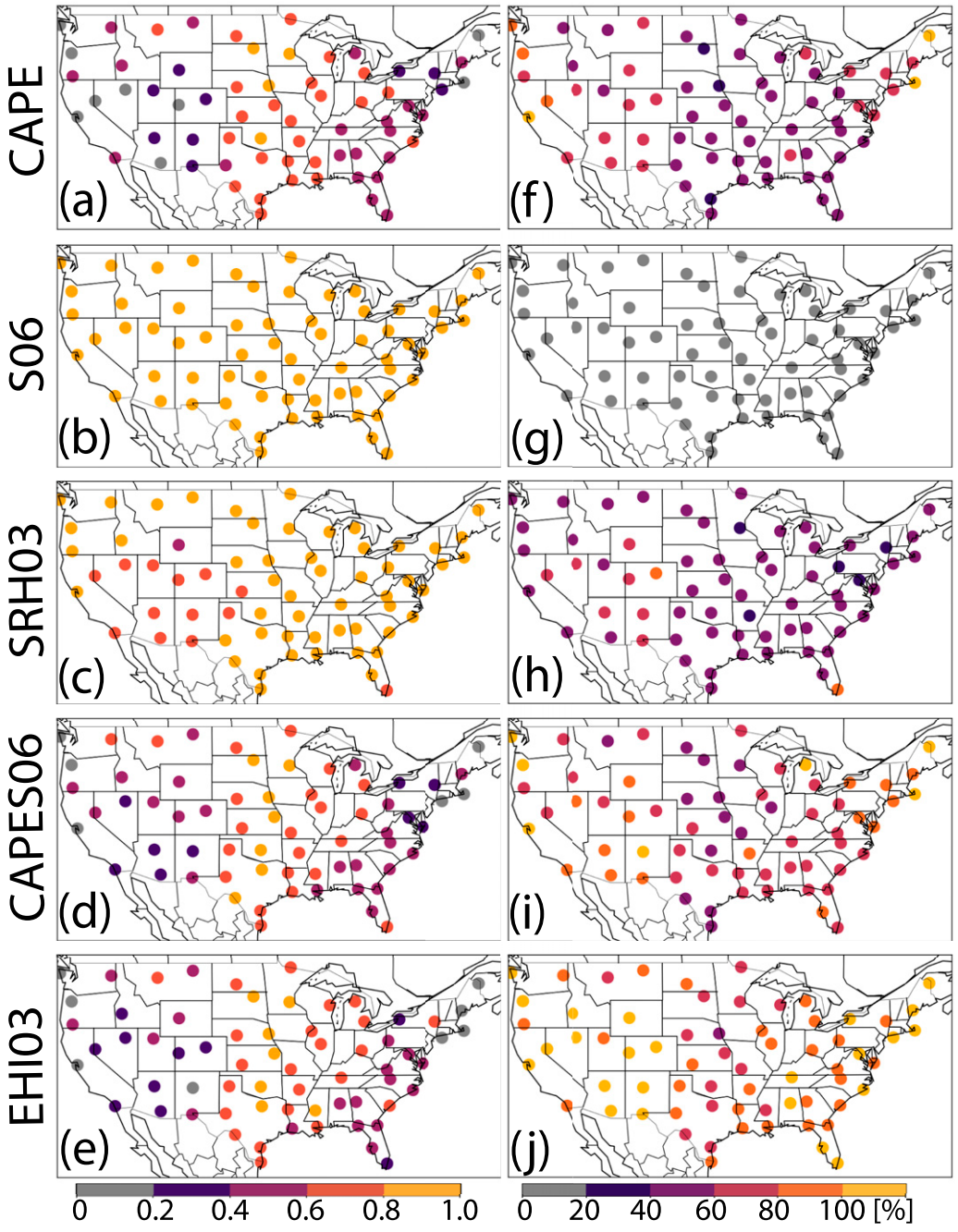

FIG. 3. ERA5 reanalysis vs radiosonde observations for the full-period (1998–2014) time series of (from top to bottom) CAPE, S06, SRH03, CAPES06, and EHI03. (a)–(e) Temporal correlation coefficient. (f)–(j) Root-mean-square error (RMSE) normalized by the local temporal mean radiosonde value. For CAPE (and thus CAPES06 and EHI03), cases with CAPE $\geq 500\ \mathrm{J\ kg^{-1}}$ from radiosonde are evaluated (sample size: Fig. S1c); S06 and SRH03 evaluation is given for all cases after quality control (sample size: Fig. S1a). ERA5 time series are generated by linearly interpolating ERA5 values onto radiosonde sites at each time step (0000 and 1200 UTC) where qualified radiosonde values exist.

Overall, ERA5 performs reasonably well in reproducing the spatiotemporal variability of key SLS environmental parameters and proxies when compared against radiosonde data, particularly east of the Rocky Mountains where SLS activity is most common. Kinematic parameters (S06 and SRH03) are generally better estimated than thermodynamic parameters (CAPE) by ERA5, particularly in the Mountain West and eastern

coasts, due to resolution limitations and associated intrinsic difficulties representing thermodynamic variability in complex terrain (Taszarek et al. 2018). This is similar to the performance of other reanalysis datasets (Gensini et al. 2014a; Taszarek et al. 2018). The temporal analysis (Fig. 3) indicate that there may be significant errors in the values of SLS environmental parameters and proxies at any given point in time at a given location. However, for climatological studies such as this work, it is the high percentiles (Fig. 2) that are most important to adequately represent.

4. Results: ERA5 and CAM6

We now move on to an in-depth analysis of SLS environments and the associated synoptic-scale features over North America in both the ERA5 reanalysis and the CAM6 historical simulation for period 1980–2014. Since ERA5 reasonably reproduces SLS environments, especially over much of the eastern half of the United States where SLS activity is most prominent, we may use ERA5 to evaluate how CAM6 reproduces these climatological environments and the associated synoptic-scale features over North America. Biases in CAM6 with respect to ERA5 are analyzed in terms of biases in the mean-state atmosphere. Additionally, common synoptic patterns that favor extreme SLS environments in regions east of the Rocky Mountains are analyzed.

a. SLS environments

We first analyze the climatology of extreme values (99th percentile) of SLS environmental proxies and parameters over North America in ERA5 and CAM6. The spatial distributions of extreme CAPES06 and EHI03 in ERA5 indicate a similar climatological pattern of such environments (Figs. 4a,b). Both extreme CAPES06 and extreme EHI03 achieve a local maximum over southern Texas and over the central United States, consistent with that in the NCEP–NCAR reanalysis dataset (Brooks et al. 2003) and radiosondes (Seeley and Romps 2015). CAM6 broadly reproduces the spatial pattern and amplitude of extreme CAPES06 and EHI03 in ERA5 (Figs. 4f,g). However, the local maximum extends farther east covering a larger area of eastern North America, with an enhancement of extreme CAPES06 and EHI03 primarily over the Upper Midwest (Figs. 4f,g and S3a,b).

CAM6 biases in extreme CAPES06 are predominantly tied to biases in extreme CAPE rather than S06, as CAM6 overestimates extreme CAPE (Figs. 4c,h and S3c) but does an excellent job in reproducing extreme S06 from ERA5 (Figs. 4d,i and S3d). Meanwhile, CAM6 biases in extreme EHI03 may be a result of biases in both extreme CAPE and SRH03, as CAM6 overestimates extreme SRH03 as well (Figs. 4e,j and S3e). Specifically, CAM6 simulates higher extreme CAPE over much of the eastern half of the United States than ERA5 does (Figs. 4c,h and S3c), and higher extreme SRH03 over the central United States and the Midwest (Figs. 4e,j and S3e); the simulated extreme S06 is nearly identical to ERA5, which attains its peak in a predominantly zonal band cutting through the central United States associated with the jet stream (Figs. 4d,i and S3d). We note that such spatial patterns of the proxies and parameters, as well as biases in CAM6 with respect to ERA5, persist across the high-percentile cases (the 95th, 90th, and 75th percentiles), though the biases decrease moving toward lower percentiles (Fig. S4).

Though not our focus in this work, convective inhibition (CIN; defined as the negative integral of buoyancy from surface to the level of free convection) is also a key parameter associated with SLS activity and environments, as it provides a measure of the lower-tropospheric stability that opposes the initiation of convection and hence release of conditional instability (Williams and Renno 1993; Chen et al. 2020). CIN extremes have a broadly similar distribution to CAPES06 and EHI extremes, and are overestimated by CAM6 as well (Fig. S5), indicative of its close linkage to CAPE. Deeper analysis of the representation of CIN in reanalysis datasets or climate models (Chen et al. 2020) may be a fruitful avenue for future work.

We next analyze the seasonal cycle. Extreme CAPES06 and EHI03 in both ERA5 and CAM6 exhibit a strong seasonal cycle that peaks in warm seasons (spring and summer) (Fig. 5), consistent with Tippett et al. (2015). Specifically, the local maximum in spring occurs over southern Texas and shifts to the central United States in summer. A similar seasonal cycle is found in extreme CAPE (Fig. 6a), whereas extreme S06 and SRH03 show an opposite seasonal phase that peaks in winter and reaches a minimum in summer (Figs. 6b,c). Biases in these SLS environments from CAM6 also exhibit a seasonal variation, as most proxies and parameters are biased higher in summer than in other seasons (Fig. S6).

Note that past work has also analyzed the number of days with significant SLS environments (NDSEV) to quantify SLS environments, such as the NDSEV with CAPES06 $\geq 10\,000\,\mathrm{m^3\,s^{-3}}$ (Brooks et al. 2003; Trapp et al. 2007, 2009; Diffenbaugh et al. 2013; Seeley and Romps 2015; Hoogewind et al. 2017) or the NDSEV with CAPES06 $\geq 20\,000\,\mathrm{m^3\,s^{-3}}$ (Gensini and Ashley 2011; Gensini et al. 2014b; Gensini and Mote 2015). The results of this method can differ from the high-percentile

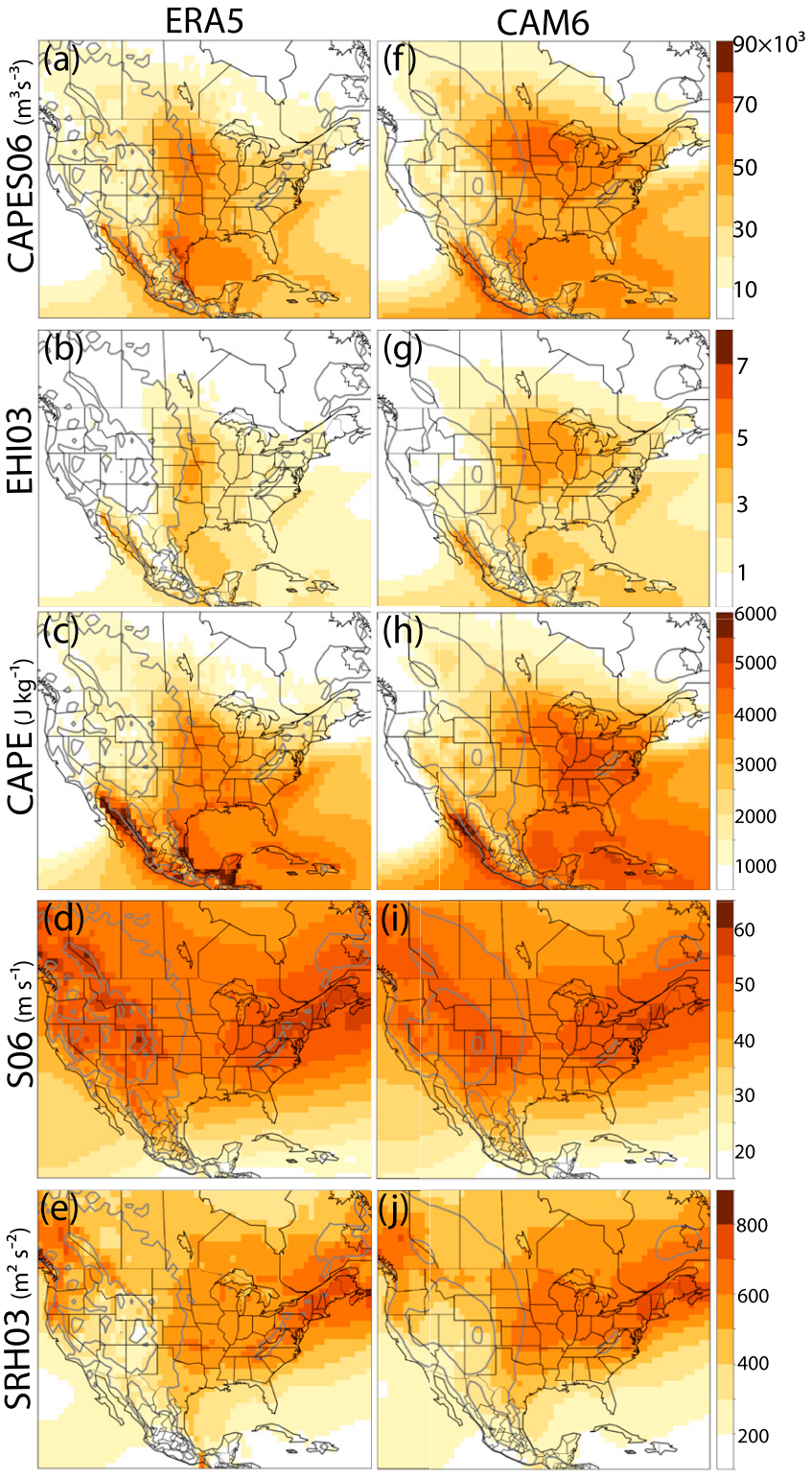

FIG. 4. ERA5 reanalysis vs CAM6 simulation for the 99th percentiles of (from top to bottom) CAPES06, EHI03, CAPE, S06, and SRH03. (a)–(e) ERA5 and (f)–(j) CAM6. The 99th percentiles are generated at each grid point from the 3-hourly full-period (1980–2014) time series. Gray contour lines denote elevations at 500, 1500, and 2500 m. Differences (CAM6 minus ERA5) are shown in Fig. S3.

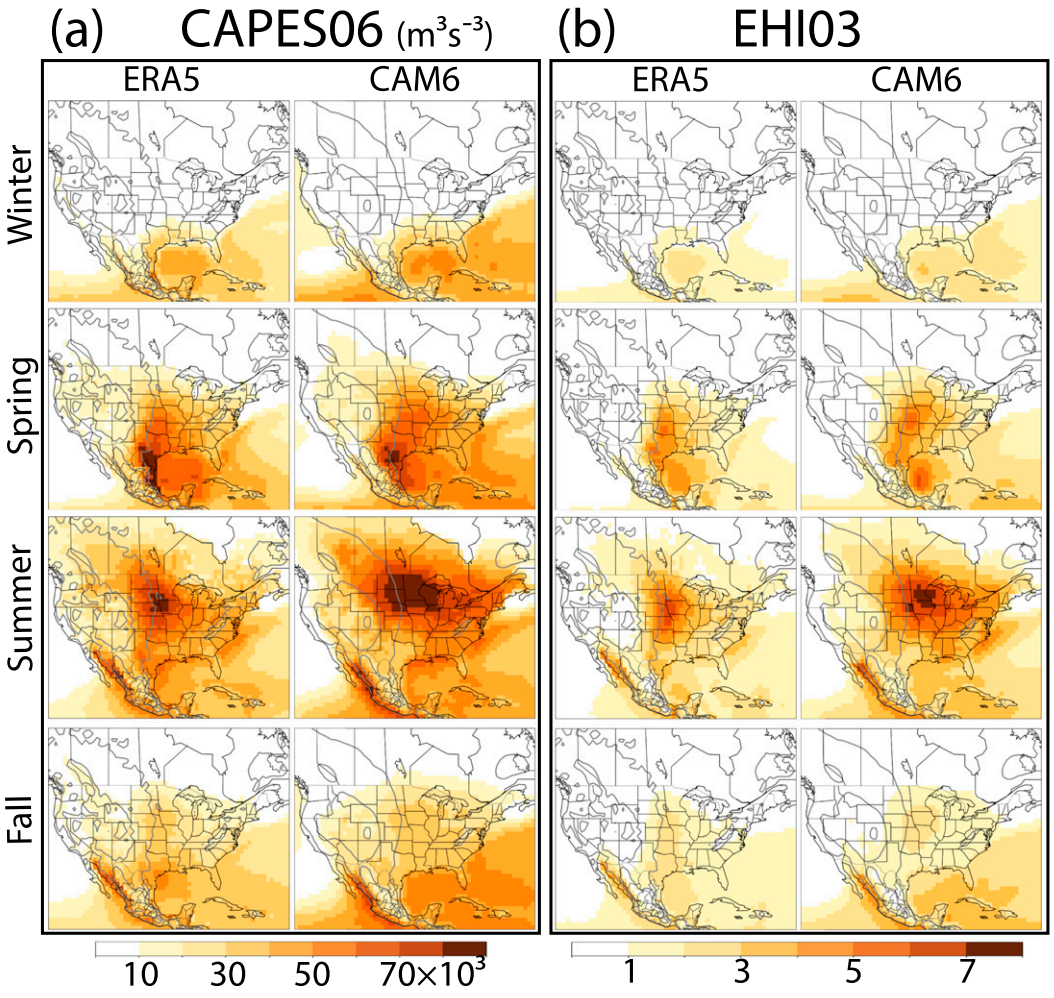

FIG. 5. ERA5 reanalysis vs CAM6 simulation for the seasonal 99th percentiles of (a) CAPES06 and (b) EHI03: (from top to bottom) winter (DJF), spring (MAM), summer (JJA), and fall (SON). The 99th percentiles are generated at each grid point from the 3-hourly full-period (1980–2014) time series during each season. Gray contour lines denote elevations at 500, 1500, and 2500 m. Differences (CAM6 minus ERA5) are shown in Figs. S6a and S6b.

method used here (Singh et al. 2017), as NDSEV is a pure frequency that does not account for the magnitude above threshold. For comparison, we calculate the climatological and seasonal cycle of NDSEV with CAPES06 exceeding 10 000 and 20 000 $m^3 s^{-3}$, respectively, in ERA5 (Fig. S7). Relative to the 99th percentile, the annual NDSEV with CAPES06 exceeding 10 000 $m^3 s^{-3}$ is shifted toward the southern United States with the local maximum confined to southern Texas (Fig. S7a), whereas distributions of the NDSEV with CAPES06 exceeding 20 000 $m^3 s^{-3}$ are broadly similar to distributions of the 99th percentile of CAPES06 (Figs. S7f–j). This is likely because cases with the lower threshold of CAPES06 are weighted more by CAPE than S06, and thus the distribution of NDSEV is dominated by that of high CAPE that both show small seasonal variations over southern Texas, especially in spring and summer (Figs. S7b–e and 6a). The NDSEV with EHI03 ≥ 1 is calculated as well, which yields a similar distribution pattern to EHI03 extremes (Figs. S7k–o).

We next analyze the diurnal cycle. Extreme CAPES06 (Fig. 7a) and EHI03 (Fig. 7b) in both ERA5 and CAM6 exhibit a strong diurnal cycle, particularly in the continental interior where the diurnal cycle peaks during the late afternoon to early evening (2100–0000 UTC) and reaches a minimum in the early morning (0900–1200 UTC). Such diurnal cycle behavior also exists along the Gulf and Atlantic coasts but with a much smaller amplitude, resembling the diurnal variation over ocean. These results are in line with past work on the diurnal variation of deep convection over North America (Wallace 1975; Nesbitt and Zipser 2003; Tian et al.

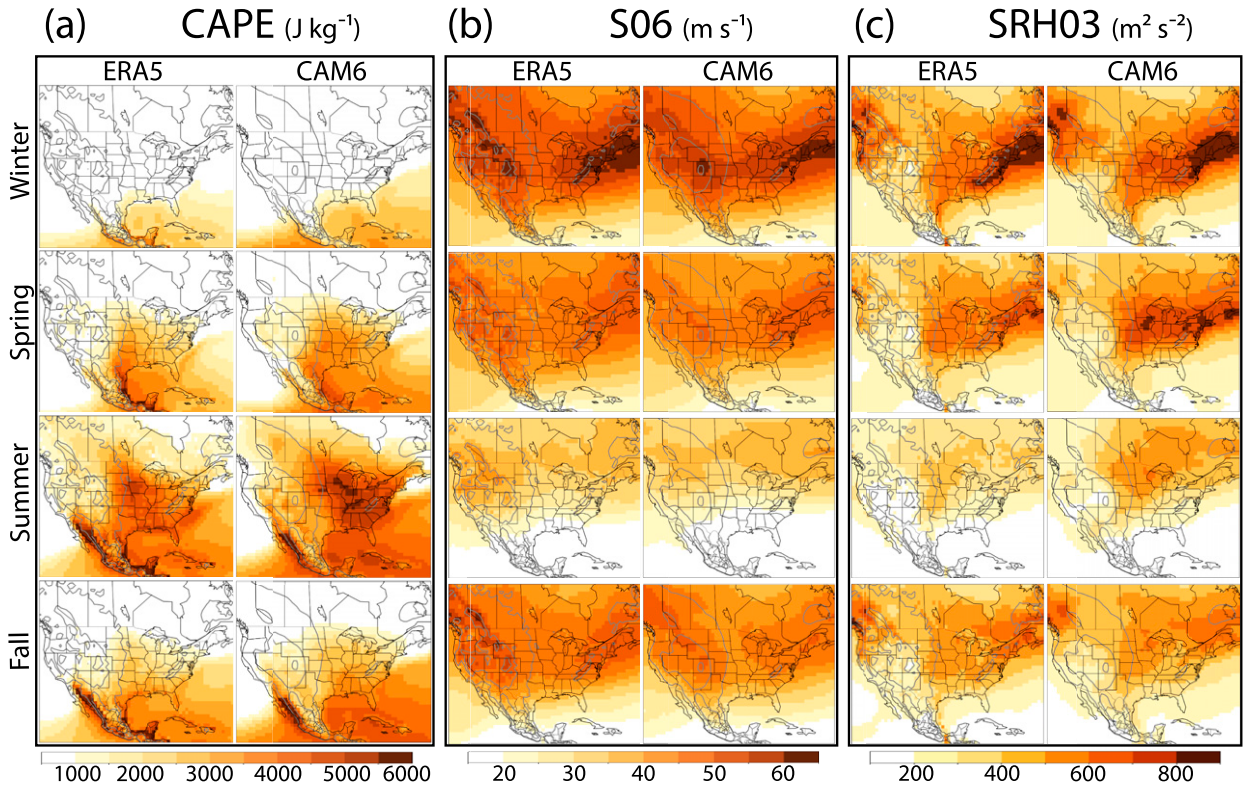

FIG. 6. As in Fig. 5, but for (a) CAPE, (b) S06, and (c) SRH03. Differences (CAM6 minus ERA5) are shown in Figs. S6c–S6e.

2005). The diurnal cycle of extreme CAPES06 and EHI03 is dominated by that of extreme CAPE (Fig. 8a), whereas the amplitude of the diurnal cycle of extreme S06 (Fig. 8b) is relatively small and extreme SRH03 peaks later (at around 0600 UTC) than extreme CAPES06 and EHI03 (Fig. 8c). The diurnal cycle signal of extreme SRH03 is strongest over the central United States, associated with the diurnal oscillation of the Great Plains low-level jets. Biases in these SLS environments from CAM6 also exhibit diurnal variations similar to the behaviors of the proxies and parameters themselves (Fig. S8).

How is extreme CAPES06 or EHI03 affected by its constituent parameters? To more precisely answer this question, we analyze the joint PDF of (CAPE, S06) and (CAPE, SRH03) within each box (R1–R6 in Fig. 1b). We analyze the entire joint distribution with special emphasis added to the top 1% cases of CAPES06 and EHI03. Both ERA5 and CAM6 indicate that the CAPES06 and EHI03 extremes consist of large-to-extreme CAPE but moderate-to-small S06 and SRH03 (Fig. 9), as was found by Diffenbaugh et al. (2013). Meanwhile, the S06 and SRH03 extremes are associated with small values of CAPE, corresponding to the high-shear, low-CAPE environments (defined as CAPE $\leq 500\,\mathrm{J\,kg^{-1}}$ and S06 $\geq 18\,\mathrm{m\,s^{-1}}$) (Guyer and Dean 2010; Sherburn and Parker 2014; Sherburn et al. 2016). These results are also evident in the seasonal cycles described above (Figs. 5, 6): high CAPES06 and EHI03 in summer are associated with very high CAPE but relatively low S06 and SRH03, while the high-shear, low-CAPE environments, corresponding to low CAPES06 and EHI03, are concentrated in winter over land. The joint PDFs also indicate that CAPES06 and EHI03 extremes are greater in CAM6 than in ERA5 for regions over the northern Great Plains (R1) and southeastern United States (R5, R6), where the joint PDF shifts toward higher (CAPE, S06) and (CAPE, SRH03). Meanwhile, the difference in the PDFs between ERA5 and CAM6 is relatively small over south-central United States (R2–R4).

b. *SLS-relevant synoptic-scale features*

1) SOUTHERLY GPLLJ

ERA5 southerly GPLLJ frequency is concentrated primarily over the central and southern Great Plains (Fig. 10a), with a seasonal frequency peak (up to 40%) in spring and summer (Figs. 10b–e). The local maximum is located in southern Texas in spring and shifts to southwestern Texas and western Oklahoma in summer,

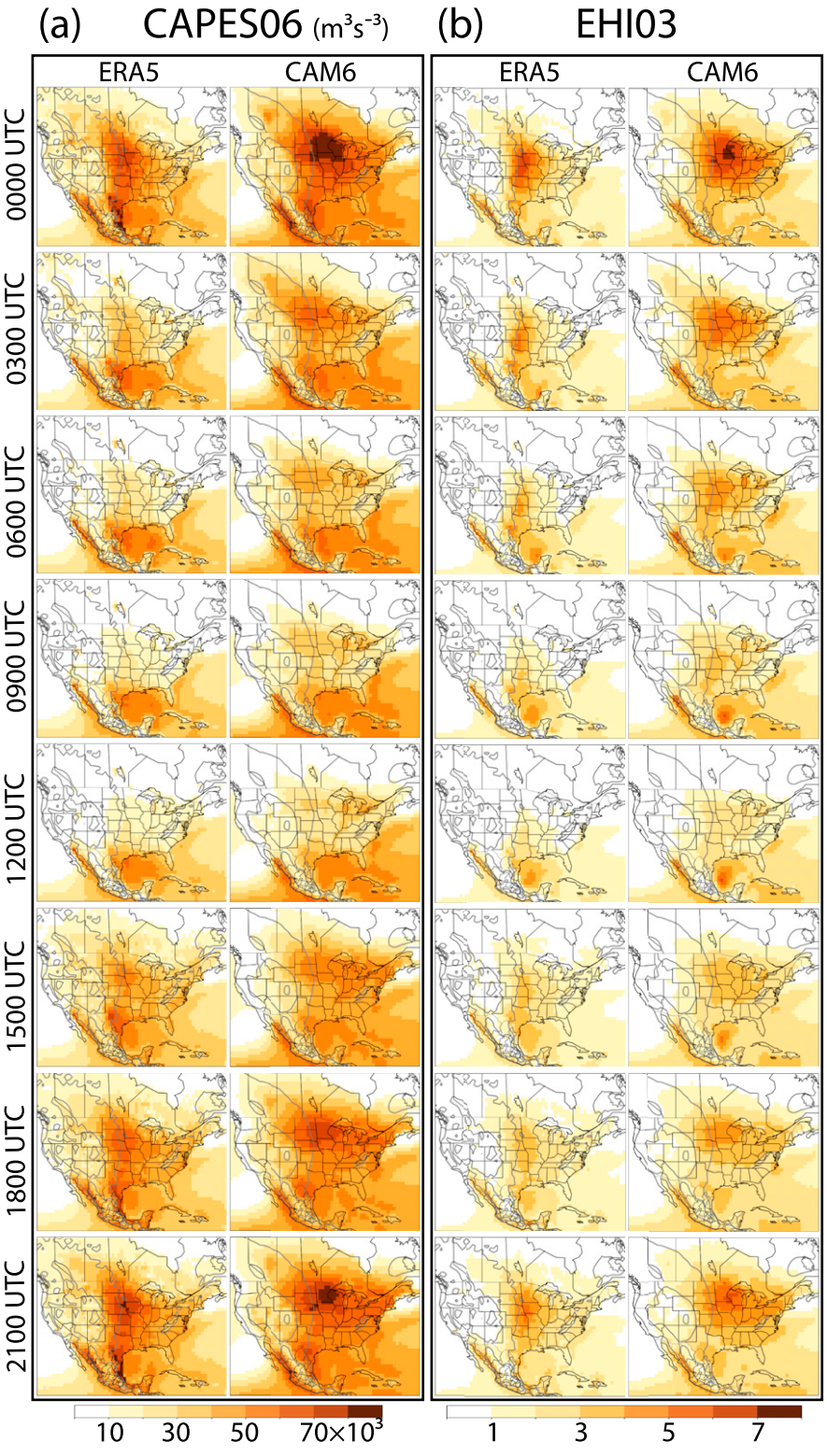

FIG. 7. ERA5 reanalysis vs CAM6 simulation for the diurnal 99th percentiles of (a) CAPES06 and (b) EHI03: (from top to bottom) 0000, 0300, 0600, 0900, 1200, 1500, 1800, and 2100 UTC. The 99th percentiles are generated at each grid point from full-period (1980–2014) time series at each 3-hourly time (UTC). Gray contour lines denote elevations at 500, 1500, and 2500 m. Differences (CAM6 minus ERA5) are shown in Figs. S8a and S8b.

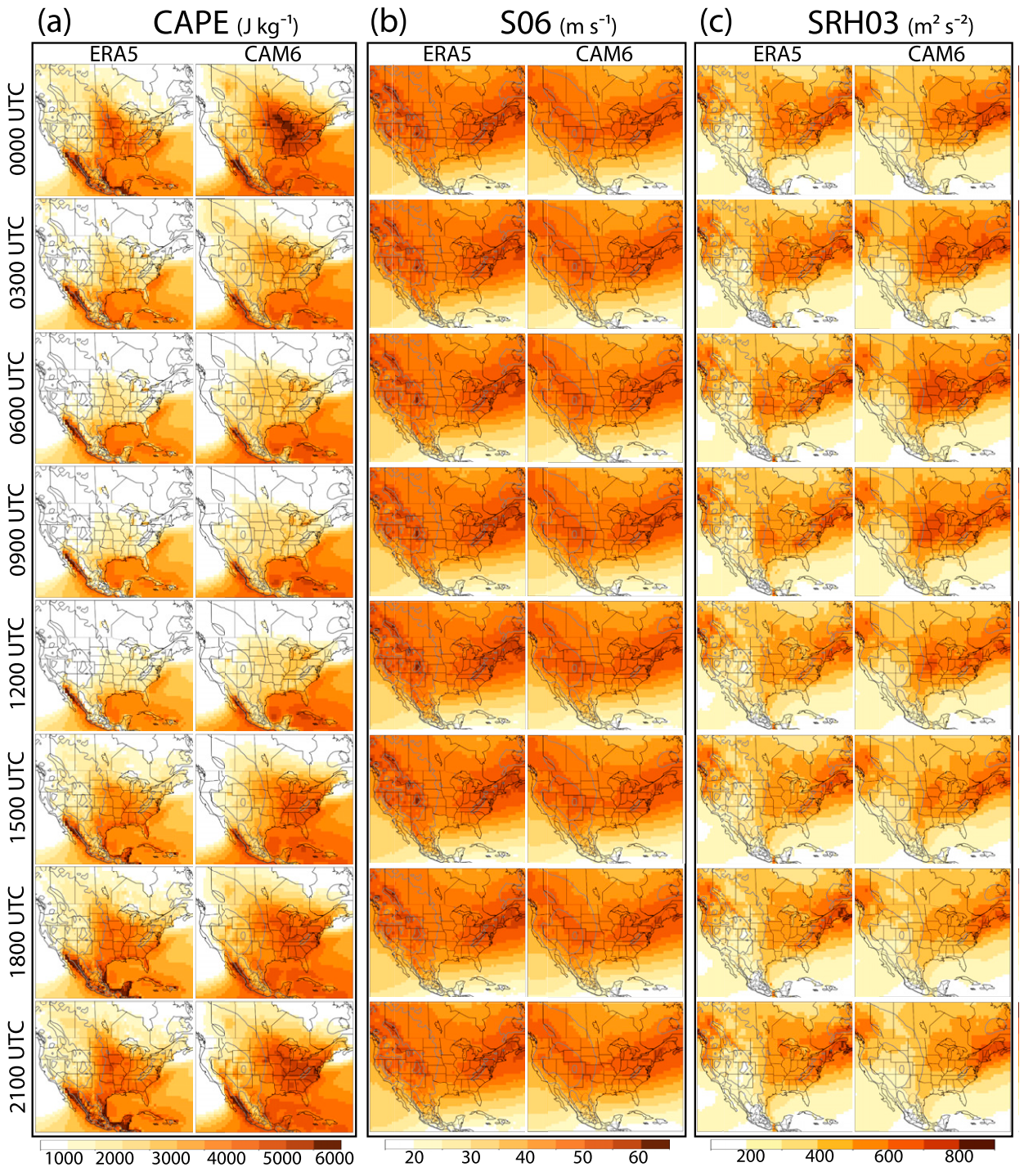

FIG. 8. As in Fig. 7, but for (a) CAPE, (b) S06, and (c) SRH03. Differences (CAM6 minus ERA5) are shown in Figs. S8c–S8e.

consistent with results of NARR reanalysis (Walters et al. 2014; Doubler et al. 2015) and observations (Bonner 1968; Walters et al. 2014). CAM6 broadly reproduces the spatial pattern and amplitude of the southerly GPLLJ frequency (Figs. 10f–j), except for summer when the frequency percentage in CAM6 (up to 50% over western Oklahoma; Fig. 10i) is much higher than that in ERA5. This increased occurrence of southerly GPLLJ indicates stronger mean low-level winds in CAM6, which may contribute to the positive biases in SRH03

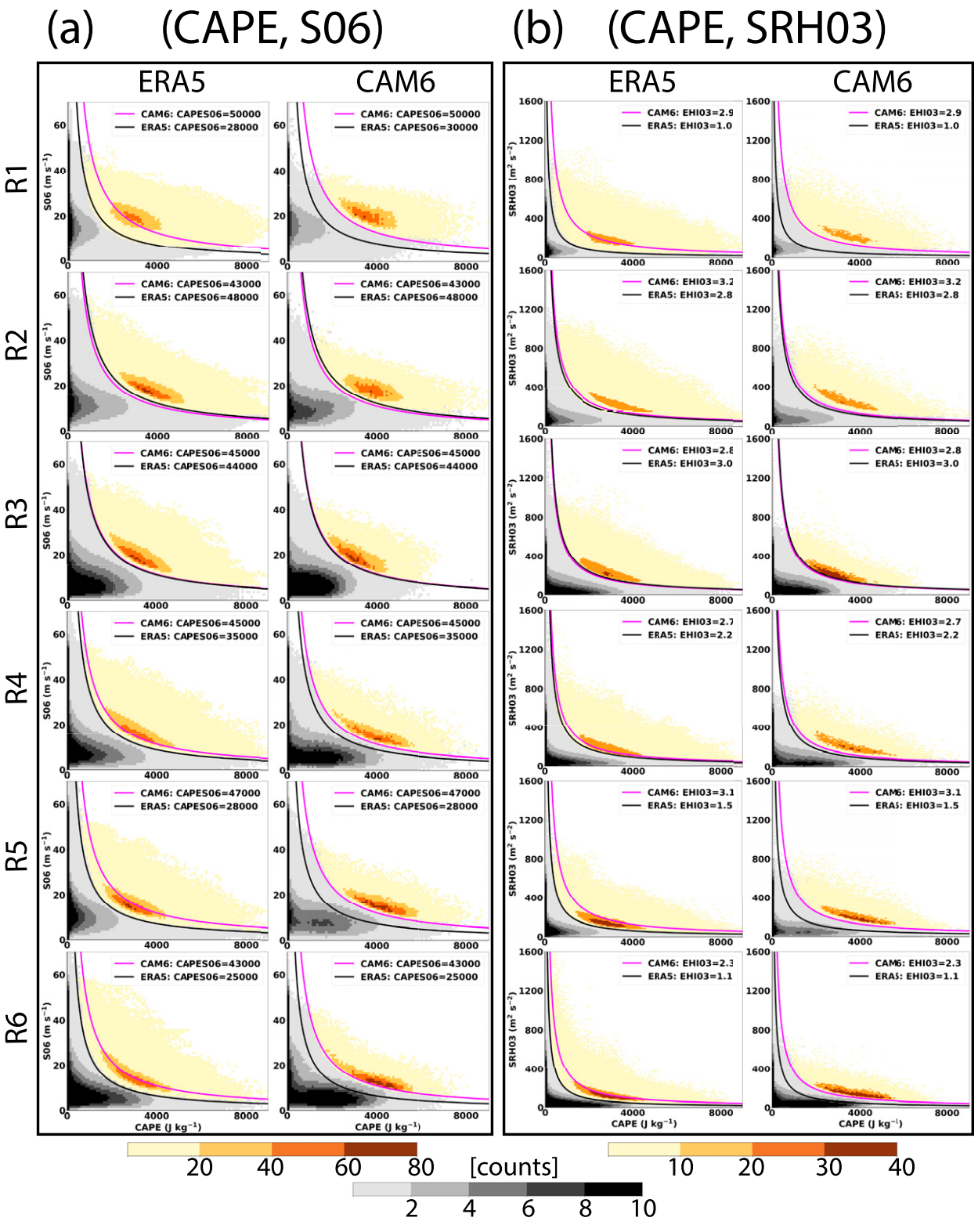

FIG. 9. ERA5 reanalysis vs CAM6 simulation for the joint probability distribution function (PDF; normalized to counts per 10 000 counts) of (a) (CAPE, S06) and (b) (CAPE, SRH03) for the top 1% cases (colors) and all cases (grays) of CAPES06 and EHI03 from 1980 to 2014, respectively, in each of the subregions R1–R6 (as defined in Fig. 1b). Solid lines represent the lower boundary of the top 1% cases (i.e., the 99th percentile) of CAPES06 or EHI03 in ERA5 (black) and CAM6 (magenta).

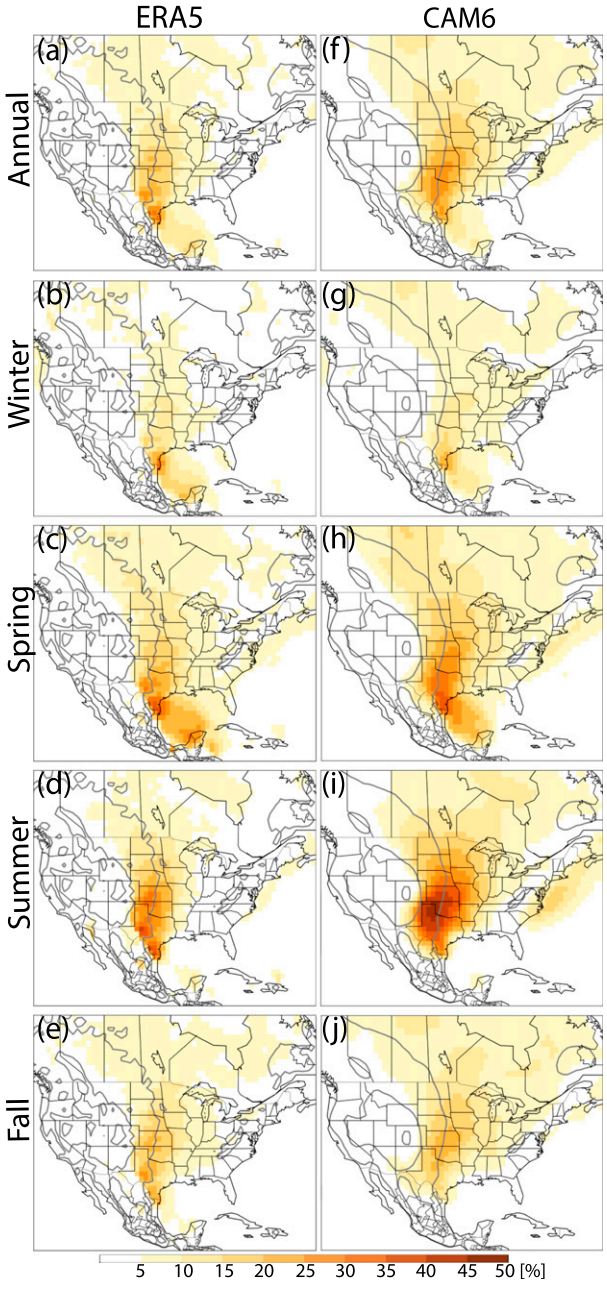

FIG. 10. ERA5 reanalysis vs CAM6 simulation for the mean frequency percentages of southerly Great Plains low-level jets during 1980–2014. For ERA5: (a) annual, (b) winter (DJF), (c) spring (MAM), (d) summer (JJA), and (e) fall (SON). (f)–(j) As in (a)–(e), but for CAM6. Gray contour lines represent elevations at 500, 1500, and 2500 m.

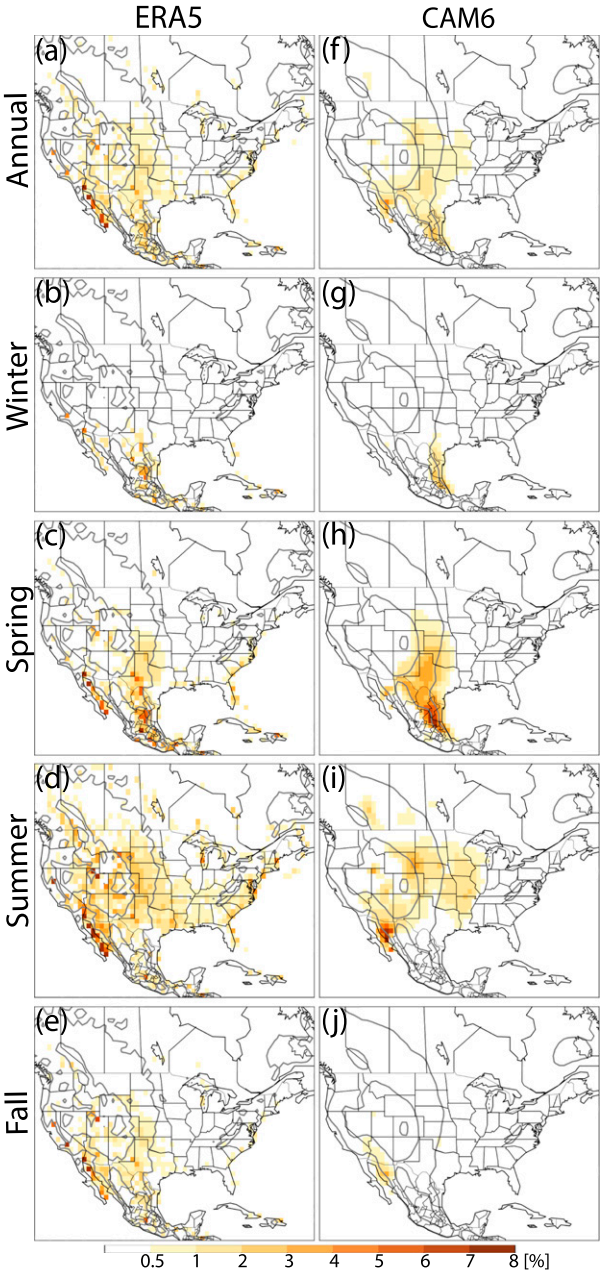

FIG. 11. As in Fig. 10, but for drylines.

over the central United States. Meanwhile, more moisture could be transported inland from the Gulf of Mexico (Helfand and Schubert 1995; Higgins et al. 1997), which may partially explain the enhanced CAPE in CAM6.

2) DRYLINE

ERA5 dryline frequency is also concentrated in the central and southern Great Plains (Fig. 11a), with a seasonal frequency peak (up to 8%) in spring over southwestern Texas (Fig. 11c). The distribution shifts poleward into the central plains in summer with a reduced frequency percentage (4%) but spanning a larger area (Fig. 11d). These results are qualitatively similar to observations by Schaefer (1974) and Hoch and Markowski

(2005), though the amplitude of dryline occurrence is lower than Hoch and Markowski (2005) owing to the stricter criteria used in this work in an effort to distinguish drylines from fronts. CAM6 performs well in reproducing the dryline distribution, as the spatial pattern and amplitude of dryline frequency over the Great Plains and its seasonal variation are broadly similar to that in ERA5 (Figs. 11f–j). ERA5 appears to better identify the less-frequent drylines over the far eastern United States (Duell and Van Den Broeke 2016), perhaps owing to its higher horizontal resolution that may permit detection of smaller-scale gradients in surface specific humidity.

3) EML

ERA5 EML frequency is again concentrated over the Great Plains (Fig. 12a), with a seasonal frequency peak in spring over the south-central United States (6%; Fig. 12c), consistent with Lanicci and Warner (1991a). The local maximum shifts poleward to South Dakota and Nebraska in summer with a reduced frequency percentage (4%; Fig. 12d), qualitatively similar to findings of Ribeiro and Bosart (2018). Note that the amplitude of EML occurrence is sensitive to the identification criteria: the criteria with 7.5 K km^{-1} for the minimum lapse rate and 150 hPa for the minimum EML depth significantly increase the frequency percentage of EML in ERA5 (e.g., 24% in spring and 20% in summer; not shown). CAM6 successfully reproduces these spatial patterns (Figs. 12f–j). However, it exhibits a significant positive bias, particularly in summer (14% over South Dakota), which is associated with the generally larger midlevel lapse rate in CAM6 than in ERA5 (detailed below in section 4c). These enhanced EMLs potentially produce more CAPE, which may also partially explain the enhanced CAPE in CAM6.

4) EXTRATROPICAL CYCLONE ACTIVITY

ERA5 cyclone track frequency has its primary local maximum to the lee of the Rocky Mountains in both the annual mean (Fig. 13a) and through the seasonal cycle (Figs. 13b–e), which is linked to cyclogenesis on the leeside of the Rocky Mountains. Secondary local maxima are also found over the Great Lakes and off the Northeastern United States coast, in line with findings of Reitan (1974) and Zishka and Smith (1980). Seasonal variation of cyclone tracks is characterized by a decrease in the frequency and a poleward shift of the local maximum from winter and spring (24 counts over southeastern Colorado) to summer (9 counts over Montana–South Dakota), qualitatively similar to past work (Reitan 1974; Zishka and Smith 1980; Eichler and Higgins 2006). Similar results are evident for EKE, as the core of EKE shifts from northwestern Oklahoma in winter to North Dakota in summer. CAM6 broadly reproduces the spatial pattern and amplitude of cyclone tracks and EKE (Figs. 13f–j). The cyclone track frequency over southeastern Colorado in CAM6 is smaller than that in ERA5 during winter, spring, and fall, likely due to the coarser horizontal resolutions (Chang et al. 2013). The major difference between CAM6 and ERA5 occurs in summer (Figs. 13d,i) when CAM6 produces more cyclone tracks and higher EKE over the central and northern Great Plains than ERA5 (roughly 21

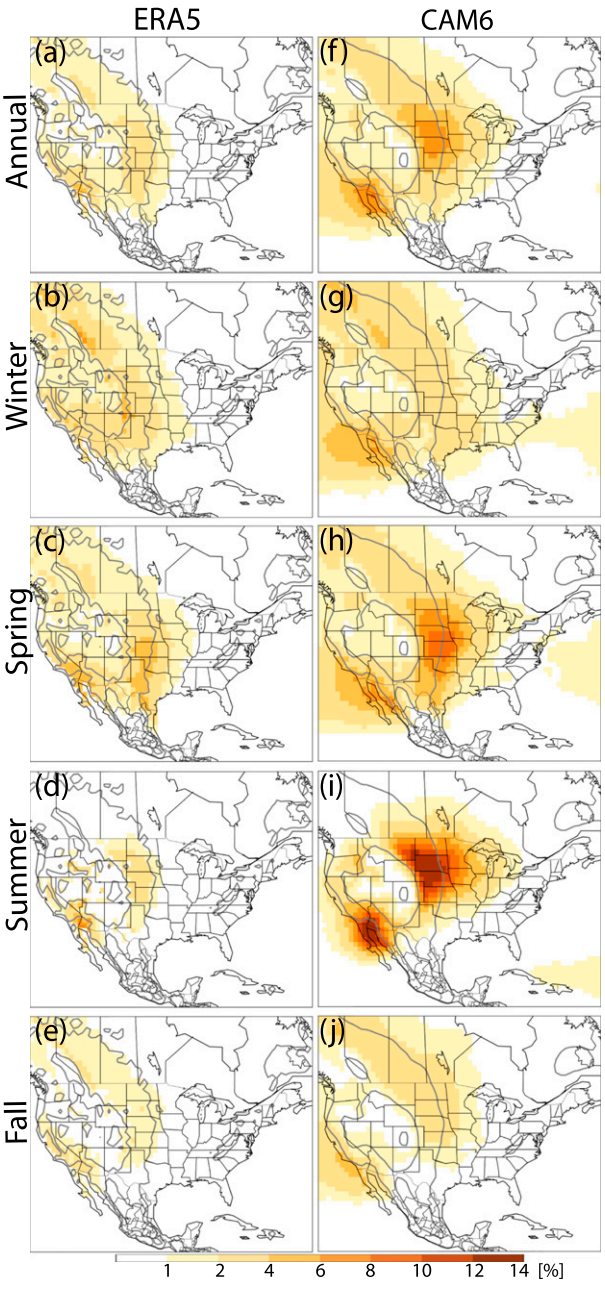

FIG. 12. As in Fig. 10, but for elevated mixed layers.

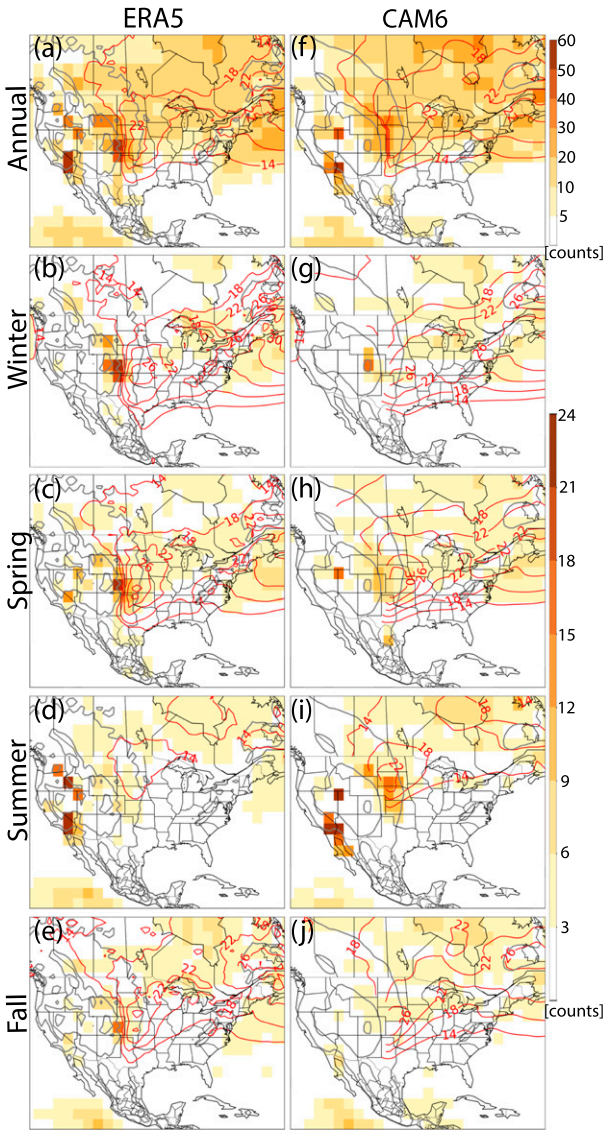

FIG. 13. As in Fig. 10, but for cyclone tracks (counts per 2.5° × 2.5° grid box; filled contours) and mean 2–6-day Butterworth bandpass-filtered eddy kinetic energy at 850 hPa ($m^2 s^{-2}$; red contour lines).

versus 9 counts and 22 versus 14 $m^2 s^{-2}$), which may contribute to the positive bias in CAM6 SLS environments in summer relative to ERA5.

Overall, both ERA5 and CAM6 produce qualitatively reasonable climatologies of the key synoptic-scale features over North America. Spatiotemporal variability in SLS environments is closely related to these synoptic-scale features: 1) both SLS environments and the associated synoptic-scale features occur typically in warm seasons (spring and summer) to the east of the Rocky Mountains, and 2) they all exhibit a poleward shift of the local maximum from winter to summer and an equatorward shift again from summer to winter. Compared with ERA5, CAM6 overestimates SLS environments, principally due to a positive bias in extreme CAPE and to a lesser degree SRH03, particularly in summer over much of the eastern half of the United States. These results are consistent with the positive bias in most synoptic-scale features (GPLLJ, EML, and extratropical cyclone activity).

c. *Biases in the mean-state atmosphere*

In an effort to better understand these biases in CAM6 relative to ERA5, we analyze differences in the mean-state atmosphere, which may provide insight into underlying causes (Trapp et al. 2007; Diffenbaugh et al. 2013). Compared to ERA5, the CAM6 summer-mean atmosphere over the eastern half of the United States (25°–49°N, 100°–62°W; Fig. 14 and S9) is characterized by higher surface and lower-tropospheric temperatures (+2 K), enhanced low- to midlevel (900–500-hPa) lapse rates [+0.5 K $(100\,hPa)^{-1}$] that accounts for the overestimated EMLs, and higher specific humidity at the surface (+0.3 g kg^{-1}) and midlevels (+0.4 g kg^{-1} averaged through 800–400 hPa). The high biases in summertime extreme CAPE and the combined proxies in CAM6 can be attributed primarily to increases in the surface specific humidity. This attribution is supported by high, statistically significant ($p < 0.001$) linear pattern correlations (r) between biases in the extreme CAPE, CAPES06, and EHI03 and biases in the surface specific humidity over the eastern half of the United States ($r = 0.81$, 0.72, and 0.80, respectively); generally small or statistically insignificant pattern correlations ($r < 0.5$) are found with biases in surface temperature, low- to midlevel lapse rate, or midlevel specific humidity.

The summer-mean wind field at the surface and the upper level in CAM6 and ERA5 is similar, though CAM6 produces a slightly stronger upper-level jet stream over southern Canada and slightly stronger surface onshore winds over Texas (Fig. S9). These outcomes help explain the relatively small biases in extreme S06. The southerly onshore winds over the Great Plains from the Gulf of Mexico are further enhanced in CAM6 at 900–850 hPa (not shown), consistent with the increased southerly GPLLJs and the positive bias of extreme SRH03 over the central Great Plains. Similar features are also evident in spring though with smaller magnitude. As for winter and fall, the difference between ERA5 and CAM6 in the mean-state atmosphere is relatively small (Fig. 14 and S9), consistent with the comparable climatologies of SLS environments and synoptic-scale features analyzed above between ERA5 and CAM6 during these seasons.

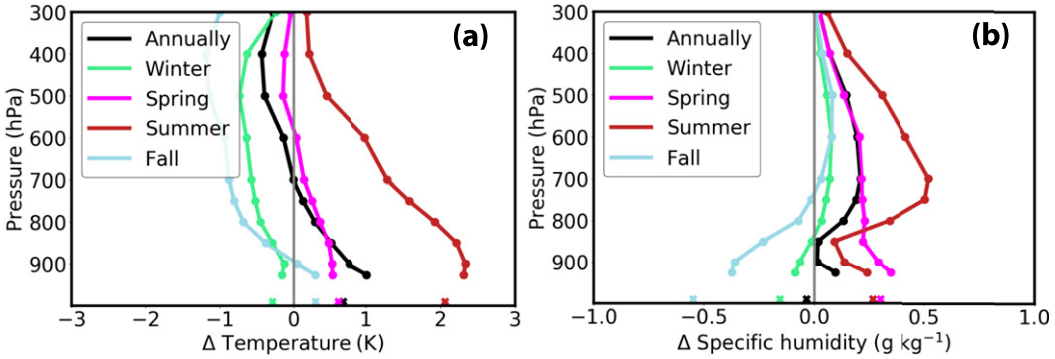

FIG. 14. Difference (CAM6 minus ERA5) in the annual and seasonal mean profiles of (a) air temperature and (b) specific humidity over the eastern half of the United States (25°–49°N, 100°–62°W) during 1980–2014. Dots denote pressure levels of 925, 900, 850, 800, 750, 700, 600, 500, 400, and 300 hPa. Cross signs indicate the difference in 2-m temperature and specific humidity.

These mean low-level warm and moist biases over the eastern half of the United States in CAM6 are associated with systematic warm and dry biases over the central United States but warm and moist biases over the eastern third of the United States (Fig. S9a). These biases have been found to persist in many generations of regional and global climate models (Klein et al. 2006; Cheruy et al. 2014; Mueller and Seneviratne 2014; Lin et al. 2017). Explanation for such systematic bias over the central United States have been proposed, including soil moisture deficit (Koster et al. 2004; Phillips and Klein 2014) or precipitation deficit (Lin et al. 2017) that alters the lower-tropospheric mean state via land–atmosphere feedback processes in climate models (Koster and Suarez 2001; Mo and Juang 2003). How precisely these systematic model biases over the eastern half of the United States affect the SLS environments and synoptic-scale features is a worthy topic left for future work.

d. Synoptic composites for extreme cases

Finally, we compare composite patterns of synoptic anomalies associated with extreme SLS environments across our subregions over the eastern half of the United States (i.e., R1–R6 defined in Fig. 1b) between ERA5 and CAM6. Here, our analysis focuses on R1 and R6. R1 is the farthest inland, over the northern Great Plains, and represents the region of the primary local maximum of SLS environments from ERA5 and CAM6; the actual SLS occurrence maximum is farther south (Agee et al. 2016). R6 is in the southeastern United States close to the Gulf of Mexico; it is known to exhibit different SLS behavior from the central United States and has shown a positive trend of SLS occurrence in recent decades (Agee et al. 2016; Gensini and Brooks 2018).

For region R1 over the eastern North Dakota and South Dakota (Fig. 15a; ERA5: 166 cases; CAM6: 92 cases), the ERA5 composite yields an enhanced ridge at 250 hPa whose axis extends from northern Texas to North Dakota, with an intensified jet streak along the U.S.–Canada border (+20–30-kt anomalies). This enhanced upper-level ridge forcing is associated with enhanced southwesterly flow at 700 hPa, which advects more warm and dry air from the elevated terrain eastward toward the Great Plains. Near the surface, the region is located on the southeast side of a trough anomaly extending southward from south-central Canada whose south-southwesterly flow has advected considerable moisture into the region. This composite pattern is similar to that found to be associated with progressive derechos (Johns 1993; Bentley et al. 2000; Guastini and Bosart 2016). CAM6 reproduces this composite pattern, though the 700-hPa warm advection is stronger and the surface trough anomaly is replaced by a slightly more intense cyclonic anomaly centered within the region.

Composite synoptic patterns for cases in the central-southern Great Plains (R2–R4) and over Indiana (R5) are broadly similar between ERA5 and CAM6, and also indicate a similar setup to that in R1, though the relative position of synoptic features varies across regions (Fig. S10). In general, an anomalous jet streak exists near the region at 250 hPa (except for R5 in CAM6 whose 250-hPa anomalies are relatively small). At 700 hPa, the region is located to the east or northeast of a warm air mass upstream, which supplies substantial warm air into the region due to the enhanced prevailing westerly or southwesterly winds. Near-surface air exhibits a deep trough or cyclonic anomaly centered to the west or northwest of the region. This results in robust advection of warm, moist air from the Gulf of Mexico into the region in

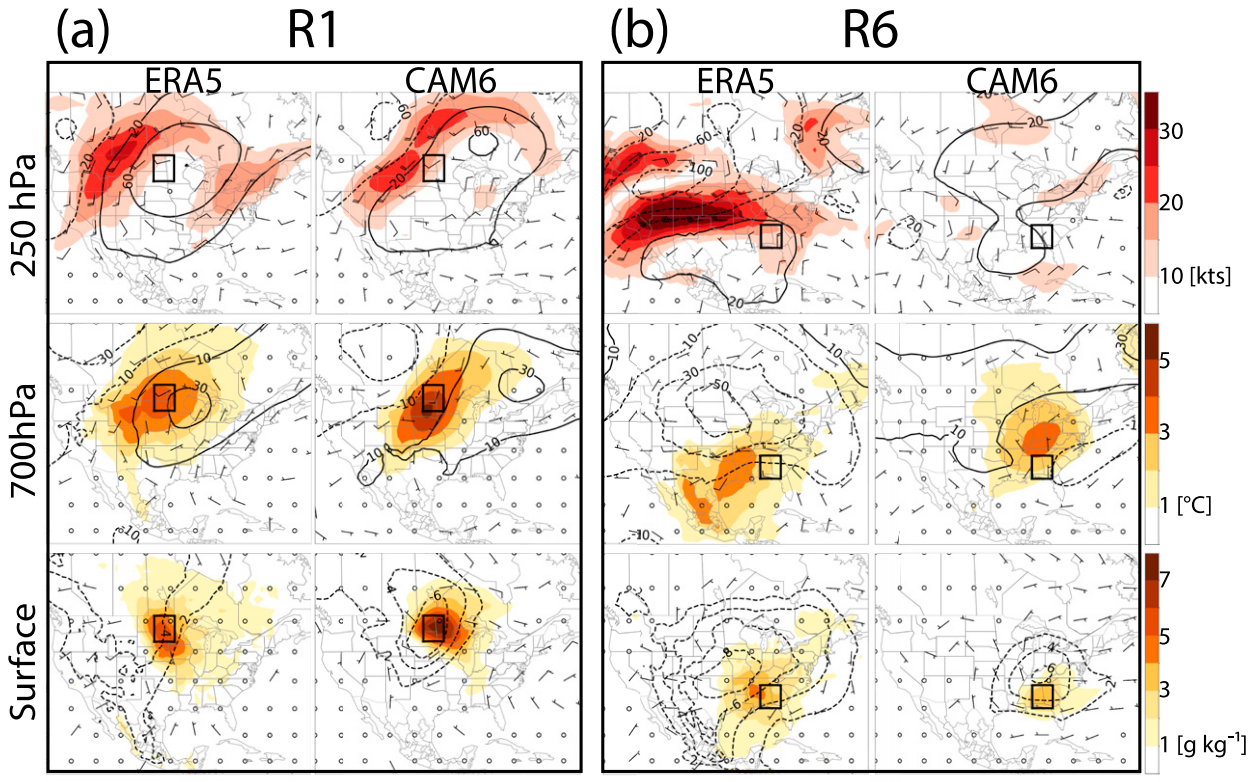

FIG. 15. ERA5 reanalysis vs CAM6 simulation for composite patterns of synoptic anomalies associated with significant SLS environments (details in the text) during 1980–2014 in regions (a) R1 and (b) R6. Black square shows the location of respective region (as defined in Fig. 1b). (top) 250 hPa, with composite anomalies of wind vector, wind speed (kt; filled contours), and geopotential height (m; black contour lines). (middle) 700 hPa, with composite anomalies of wind vector, temperature (°C; filled contours), and geopotential height (m; black contour lines). (bottom) Near surface, with composite anomalies of 10-m wind vector, 2-m specific humidity (g kg^{-1}; filled contours), and sea level pressure (hPa; black contour lines). Composite synoptic anomalies for subregions of R2–R5 are shown in Fig. S10.

the lower troposphere. These synoptic composites are broadly similar to the classic patterns of severe weather outbreaks over the Great Plains (Barnes and Newton 1986; Johns and Doswell 1992; Johns 1993; Mercer et al. 2012).

The synoptic composite for subregion R6 over the southeastern United States (Fig. 15b; ERA5: 40 cases; CAM6: 96 cases) differs from the other subregions as well as between ERA5 and CAM6. The ERA5 composite yields a much more intense jet stream (anomaly $\geq$ 30 kt) over the central United States at 250 hPa and a subtle shortwave trough at 700 hPa. Near the surface, a strong extratropical cyclone occupies much of the eastern half of North America with a low pressure anomaly centered over the central United States. The region (R6) is located to the southeast of the surface low. One key difference from the other regions is that this area is directly influenced by the flow on the west side of the North Atlantic subtropical high, which enhances the southwesterly low-level winds and moisture advection over the region (Stahle and Cleaveland 1992; Miller and Mote 2017). The CAM6 composite reproduces this near-surface flow pattern, but at higher levels it yields a broad ridge at 250- and 700-hPa and without any anomalous jet streak enhancement to the northwest of the region at 250 hPa. The surface cyclonic anomaly is weaker in CAM6 than in ERA5, transporting less moisture into the region.

Overall, the common synoptic anomaly patterns associated with extreme SLS environments show small variations across subregions over much of the eastern half of the United States (R1–R5), where CAM6 also compares well with ERA5. The southeastern United States (R6) behavior differs somewhat from the other regions, as well as between ERA5 and CAM6, which indicates differences in the generation of SLS environments in the Southeast as compared to farther inland. The SLS environments in the Southeast involve a significant portion of high-shear, low-CAPE environments (Guyer and Dean 2010; Sherburn and Parker 2014; Sherburn et al. 2016), which are known to be associated with more difficult forecasting of SLS activity (Miller and Mote 2017). This also implies that the extreme

CAPES06 or EHI03 used may be not broadly applicable to identify SLS environments over the Southeast, as they in general capture high-CAPE environments while miss high-shear low-CAPE cases (Fig. 9), and thus the composite synoptic patterns for R6 may be less representative of the SLS events in the Southeast. Sufficient low-level moisture supply is clearly essential for generating SLS environments, as all composite analyses reveal robust moisture transport at low levels. Deeper composite analysis using other composite methods such as empirical orthogonal functions (EOFs; Schaefer and Doswell 1984), rotated principal component analysis (RPCA; Jones et al. 2004; Mercer et al. 2012), or self-organizing maps (SOMs; Sheridan and Lee 2011) would be a valuable path for future work.

5. Conclusions

This work provides a comprehensive climatological analysis and evaluation of SLS environments, and the associated synoptic-scale features that frequently generate them, in the ERA5 reanalysis dataset and CAM6 climate model simulation. Unlike reanalysis datasets, climate models do not reproduce the observed daily weather, but they both are capable of capturing statistical properties (e.g., the mean or extremes) of a climate state. Thus, we analyzed the overall climatology, as well as seasonal and diurnal cycles, of SLS environments and the occurrence frequency of relevant synoptic-scale features in the ERA5 reanalysis and a CAM6 AMIP-style simulation for the period 1980–2014 over North America. Here, SLS environments are measured by extreme values (defined as the 99th percentile) of two environmental proxies for SLS favorability, CAPES06 (the product of CAPE and S06) and EHI03 (proportional to the product of CAPE and SRH03), as well as their constituent parameters (CAPE, S06, and SRH03). Key synoptic-scale features commonly associated with the generation of SLS environments analyzed in this work include southerly Great Plains low-level jets, drylines, elevated mixed layers, and extratropical cyclone activity. Biases in these SLS environments and synoptic-scale features from CAM6 were attributed to biases in the mean-state atmosphere. Finally, composite analysis was conducted for six subregions over the eastern half of the United States to characterize the common synoptic patterns associated with significant SLS environments and assess their CAM6 representation as compared to ERA5.

The primary results of our study are summarized as follows:

1) ERA5 reasonably reproduces the observed (radiosonde) spatiotemporal distribution of SLS environments, with relatively low biases and strong correlations particularly over the Great Plains. Kinematic parameters (S06 and SRH03) are in general better estimated by ERA5 than thermodynamic parameters (CAPE), especially for stations in the Mountain West and along the east coast where terrain effects are likely large.
2) Climatological patterns of extreme SLS environments over North America are reasonably well captured by ERA5 and CAM6. Both ERA5 and CAM6 representations of extreme CAPES06 and EHI03 indicate qualitatively similar annual, seasonal, and diurnal climatologies of SLS environments. Local maxima are found over southern Texas in spring and shift to the north-central United States in summer. The diurnal cycle peaks during the late afternoon and early evening with a minimum in the early morning, with larger amplitude over the continental interior and smaller amplitude in coastal regions. Extreme values of CAPES06 or EHI03 typically consist of very high CAPE and moderate-to-small S06 or SRH03, and thus the climatological behavior of these combined proxies are dominated by the behavior of CAPE extremes, not S06 or SRH03 extremes. This implies that extreme CAPES06 and EHI03 is less representative of high-shear, low-CAPE environments that contribute to a considerable portion of SLS environments in the southeastern United States.
3) Climatologies of key synoptic-scale features over North America are reasonably captured by ERA5 and CAM6 as well. Southerly Great Plains low-level jets, drylines, elevated mixed layers, and extratropical cyclone activity in both ERA5 and CAM6 are most frequent east of the Rocky Mountains in warm seasons. Both ERA5 and CAM6 capture the strong linkage between SLS environments and these synoptic-scale features, as the spatial pattern and seasonal variation of the occurrence frequency of these synoptic-scale features are highly consistent with that of SLS environments.
4) Biases in CAM6 relative to ERA5 over the eastern United States are largest during summer: 1) CAPE extremes are biased high in CAM6 over much of the eastern half of the United States, which is primarily attributed to the enhanced mean surface specific humidity in CAM6; 2) SRH03 extremes are biased slightly high, which is primarily attributed to the stronger mean-state low-level winds in CAM6 than ERA5 and more frequent southerly Great Plains low-level jets; 3) elevated mixed-layer frequency is biased high, which is primarily attributed to a steeper mean-state midlevel lapse rate and further enhances

CAPE; and 4) taken together, the combined proxies CAPES06 and EHI03 are each biased high.

5) The composite synoptic patterns favorable for extreme SLS environments within six subregions across the eastern half of the United States in ERA5 indicate an intensified upper-level jet streak in the vicinity of the region, strong warm and dry air advection from upstream elevated terrain eastward over the Great Plains, and robust low-level moisture transport from the Gulf of Mexico due to the enhanced prevailing southerly or southwesterly winds east of a surface trough or cyclonic anomaly. CAM6 successfully reproduces these structures found in ERA5 for most regions. The principal exception is over the southeastern United States in CAM6 where the influence of the North Atlantic subtropical high is also important, highlighting differences in climatological forcing that may translate to different behavior and predictability of severe weather itself, as has been identified in past work.

These results suggest that the ERA5 reanalysis reasonably reproduce SLS environments and the relevant synoptic-scale features, and climate models such as CAM6 can be useful tools to investigate climate controls on the generation of SLS environments over North America. Meanwhile, it is necessary to be aware of the biases in climate models (e.g., the systematic biases in surface moisture and temperature over the central and eastern United States), which may directly impact SLS environments and hence affect the interpretation of their responses to climate forcing. To further understand the formation of SLS environments within climate system, future work can use idealized climate modeling experiments to quantitatively test both the detailed linkages between key synoptic-scale features and SLS environments, as well as how climate-scale boundary forcing fundamentally controls the spatiotemporal distribution of SLS environments on Earth.

Acknowledgments. The authors thank Larry Oolman (University of Wyoming) for providing radiosonde data. The authors thank Editor Dr. Xin-Zhong Liang and three anonymous reviewers for their feedback in improving this manuscript. The authors would like to acknowledge high-performance computing support from Cheyenne (doi:10.5065/D6RX99HX) provided by NCAR's Computational and Information Systems Laboratory, sponsored by the National Science Foundation, for the simulation and data analysis performed for this work. This research was also supported in part through computational resources provided by Information Technology at Purdue, West Lafayette, Indiana. Li, Chavas, and Reed were supported by NSF Grant AGS1648681. Reed was also supported by NSF Grant AGS1648629 and the U.S. Department of Energy Office of Science (DE-SC0019459).

REFERENCES

Agee, E., J. Larson, S. Childs, and A. Marmo, 2016: Spatial redistribution of U.S. tornado activity between 1954 and 2013. *J. Appl. Meteor. Climatol.*, **55**, 1681–1697, https://doi.org/10.1175/JAMC-D-15-0342.1.

Allen, J. T., and D. J. Karoly, 2014: A climatology of Australian severe thunderstorm environments 1979–2011: Inter-annual variability and ENSO influence. *Int. J. Climatol.*, **34**, 81–97, https://doi.org/10.1002/joc.3667.

Banacos, P. C., and M. L. Ekster, 2010: The association of the elevated mixed layer with significant severe weather events in the northeastern United States. *Wea. Forecasting*, **25**, 1082–1102, https://doi.org/10.1175/2010WAF2222363.1.

Barnes, S., and C. Newton, 1986: Thunderstorms in the synoptic setting. *ThunderStorms: A Social, Scientific, and Technological Documentary. Vol. 2: Thunderstorm Morphology and Dynamics*, 2nd ed. E. Kessler, Ed., University of Oklahoma Press, 75–111.

Bentley, M. L., T. L. Mote, and S. F. Byrd, 2000: A synoptic climatology of derecho producing mesoscale convective systems in the North-Central Plains. *Int. J. Climatol.*, **20**, 1329–1349, https://doi.org/10.1002/1097-0088(200009)20:11%3C1329::AID-JOC537%3E3.0.CO;2-F.

Blackmon, M. L., 1976: A climatological spectral study of the 500 mb geopotential height of the Northern Hemisphere. *J. Atmos. Sci.*, **33**, 1607–1623, https://doi.org/10.1175/1520-0469(1976)033<1607:ACSSOT>2.0.CO;2.

Blumberg, W. G., K. T. Halbert, T. A. Supinie, P. T. Marsh, R. L. Thompson, and J. A. Hart, 2017: SHARPpy: An open-source sounding analysis toolkit for the atmospheric sciences. *Bull. Amer. Meteor. Soc.*, **98**, 1625–1636, https://doi.org/10.1175/BAMS-D-15-00309.1.

Bogenschutz, P. A., A. Gettelman, H. Morrison, V. E. Larson, C. Craig, and D. P. Schanen, 2013: Higher-order turbulence closure and its impact on climate simulations in the Community Atmosphere Model. *J. Climate*, **26**, 9655–9676, https://doi.org/10.1175/JCLI-D-13-00075.1.

Bonner, W. D., 1968: Climatology of the low level jet. *Mon. Wea. Rev.*, **96**, 833–850, https://doi.org/10.1175/1520-0493(1968)096<0833:COTLLJ>2.0.CO;2.

Brooks, H. E., J. W. Lee, and J. P. Craven, 2003: The spatial distribution of severe thunderstorm and tornado environments from global reanalysis data. *Atmos. Res.*, **67**, 79–94, https://doi.org/10.1016/S0169-8095(03)00045-0.

Bunkers, M. J., B. A. Klimowski, J. W. Zeitler, R. L. Thompson, and M. L. Weisman, 2000: Predicting supercell motion using a new hodograph technique. *Wea. Forecasting*, **15**, 61–79, https://doi.org/10.1175/1520-0434(2000)015<0061:PSMUAN>2.0.CO;2.

Carlson, T. N., S. G. Benjamin, G. S. Forbes, and Y. F. Li, 1983: Elevated mixed layers in the regional severe storm environment: Conceptual model and case studies. *Mon. Wea. Rev.*, **111**, 1453–1474, https://doi.org/10.1175/1520-0493(1983)111<1453:EMLITR>2.0.CO;2.

Chang, E. K., Y. Guo, X. Xia, and M. Zheng, 2013: Storm-track activity in IPCC AR4/CMIP3 model simulations. *J. Climate*, **26**, 246–260, https://doi.org/10.1175/JCLI-D-11-00707.1.

Chen, J., A. Dai, Y. Zhang, and K. L. Rasmussen, 2020: Changes in convective available potential energy and convective inhibition under global warming. *J. Climate*, **33**, 2025–2050, https://doi.org/10.1175/JCLI-D-19-0461.1.

Cheruy, F., J. Dufresne, F. Hourdin, and A. Ducharne, 2014: Role of clouds and land-atmosphere coupling in midlatitude continental summer warm biases and climate change amplification in CMIP5 simulations. *Geophys. Res. Lett.*, **41**, 6493–6500, https://doi.org/10.1002/2014GL061145.

Cordeira, J. M., N. D. Metz, M. E. Howarth, and T. J. Galarneau Jr., 2017: Multiscale upstream and in situ precursors to the elevated mixed layer and high-impact weather over the Midwest United States. *Wea. Forecasting*, **32**, 905–923, https://doi.org/10.1175/WAF-D-16-0122.1.

Davies-Jones, R. P., 1993: Helicity trends in tornado outbreaks. Preprints, *17th Conf. on Severe Local Storms*, St. Louis, MO, Amer. Meteor. Soc., 56–60.

——, 2002: Linear and nonlinear propagation of supercell storms. *J. Atmos. Sci.*, **59**, 3178–3205, https://doi.org/10.1175/1520-0469(2003)059<3178:LANPOS>2.0.CO;2.

——, 2003: Reply. *J. Atmos. Sci.*, **60**, 2420–2426, https://doi.org/10.1175/1520-0469(2003)060<2420:R>2.0.CO;2.

——, D. Burgess, and M. Foster, 1990: Test of helicity as a tornado forecast parameter. Preprints, *16th Conf. on Severe Local Storms,* Kananaskis Park, AB, Canada, Amer. Meteor. Soc., 588–592.

Dee, D. P., and Coauthors, 2011: The ERA-Interim reanalysis: Configuration and performance of the data assimilation system. *Quart. J. Roy. Meteor. Soc.*, **137**, 553–597, https://doi.org/10.1002/qj.828.

Diffenbaugh, N. S., M. Scherer, and R. J. Trapp, 2013: Robust increases in severe thunderstorm environments in response to greenhouse forcing. *Proc. Natl. Acad. Sci. USA*, **110**, 16 361–16 366, https://doi.org/10.1073/pnas.1307758110.

Doswell, C. A., III, and D. W. Burgess, 1993: Tornadoes and tornadic storms: A review of conceptual models. *The Tornado: Its Structure, Dynamics, Hazards, and Prediction, Geophys. Monogr.,* Vol. 79, Amer. Geophys. Union, https:doi.org/10.1029/GM079p0161.

——, and E. N. Rasmussen, 1994: The effect of neglecting the virtual temperature correction on CAPE calculations. *Wea. Forecasting*, **9**, 625–629, https://doi.org/10.1175/1520-0434(1994)009<0625:TEONTV>2.0.CO;2.

——, and L. F. Bosart, 2001: Extratropical synoptic-scale processes and severe convection. *Severe Convective Storms*, C. A. Doswell, Ed., Springer, 27–69, https://doi.org/10.1007/978-1-935704-06-5_2.

——, and D. M. Schultz, 2006: On the use of indices and parameters in forecasting severe storms. *Electron. J. Severe Storms Meteor.*, **1** (3), https://ejssm.org/ojs/index.php/ejssm/article/viewarticle/11/12.

Doubler, D. L., J. A. Winkler, X. Bian, C. K. Walters, and S. Zhong, 2015: An NARR-derived climatology of southerly and northerly low-level jets over North America and coastal environs. *J. Appl. Meteor. Climatol.*, **54**, 1596–1619, https://doi.org/10.1175/JAMC-D-14-0311.1.

Duell, R. S., and M. S. Van Den Broeke, 2016: Climatology, synoptic conditions, and misanalyses of Mississippi River Valley drylines. *Mon. Wea. Rev.*, **144**, 927–943, https://doi.org/10.1175/MWR-D-15-0108.1.

ECMWF, 2019: ERA5 Reanalysis (0.25 Degree Latitude-Longitude Grid). Research Data Archive at the National Center for Atmospheric Research, Computational and Information Systems Laboratory, accessed 19 September 2019, https://doi.org/10.5065/BH6N-5N20.

Eichler, T., and W. Higgins, 2006: Climatology and ENSO-related variability of North American extratropical cyclone activity. *J. Climate*, **19**, 2076–2093, https://doi.org/10.1175/JCLI3725.1.

Eyring, V., S. Bony, G. A. Meehl, C. A. Senior, B. Stevens, R. J. Stouffer, and K. E. Taylor, 2016: Overview of the Coupled Model Intercomparison Project phase 6 (CMIP6) experimental design and organization. *Geosci. Model Dev.*, **9**, 1937–1958, https://doi.org/10.5194/gmd-9-1937-2016.

Farrell, R. J., and T. N. Carlson, 1989: Evidence for the role of the lid and underrunning in an outbreak of tornadic thunderstorms. *Mon. Wea. Rev.*, **117**, 857–871, https://doi.org/10.1175/1520-0493(1989)117<0857:EFTROT>2.0.CO;2.

Fujita, T., 1958: Structure and movement of a dry front. *Bull. Amer. Meteor. Soc.*, **39**, 574–582, https://doi.org/10.1175/1520-0477-39.11.574.

Gates, W. L., and Coauthors, 1999: An overview of the results of the Atmospheric Model Intercomparison Project (AMIP I). *Bull. Amer. Meteor. Soc.*, **80**, 29–55, https://doi.org/10.1175/1520-0477(1999)080<0029:AOOTRO>2.0.CO;2.

Gensini, V. A., and W. S. Ashley, 2011: Climatology of potentially severe convective environments from the North American regional reanalysis. *J. Severe Storms Meteor.*, **6**, 1–40.

——, and T. L. Mote, 2014: Estimations of hazardous convective weather in the United States using dynamical downscaling. *J. Climate*, **27**, 6581–6589, https://doi.org/10.1175/JCLI-D-13-00777.1.

——, and ——, 2015: Downscaled estimates of late 21st century severe weather from CCSM3. *Climatic Change*, **129**, 307–321, https://doi.org/10.1007/s10584-014-1320-z.

——, and H. E. Brooks, 2018: Spatial trends in United States tornado frequency. *npj Climate Atmos. Sci.*, **1**, 38, https://doi.org/10.1038/s41612-018-0048-2.

——, and L. Bravo de Guenni, 2019: Environmental covariate representation of seasonal U.S. tornado frequency. *J. Appl. Meteor. Climatol.*, **58**, 1353–1367, https://doi.org/10.1175/JAMC-D-18-0305.1.

——, T. L. Mote, and H. E. Brooks, 2014a: Severe-thunderstorm reanalysis environments and collocated radiosonde observations. *J. Appl. Meteor. Climatol.*, **53**, 742–751, https://doi.org/10.1175/JAMC-D-13-0263.1.

——, C. Ramseyer, and T. L. Mote, 2014b: Future convective environments using NARCCAP. *Int. J. Climatol.*, **34**, 1699–1705, https://doi.org/10.1002/joc.3769.

Gettelman, A., and H. Morrison, 2015: Advanced two-moment bulk microphysics for global models. Part I: Off-line tests and comparison with other schemes. *J. Climate*, **28**, 1268–1287, https://doi.org/10.1175/JCLI-D-14-00102.1.

Golaz, J.-C., V. E. Larson, and W. R. Cotton, 2002: A PDF-based model for boundary layer clouds. Part I: Method and model description. *J. Atmos. Sci.*, **59**, 3540–3551, https://doi.org/10.1175/1520-0469(2002)059<3540:APBMFB>2.0.CO;2.

Grams, J. S., R. L. Thompson, D. V. Snively, J. A. Prentice, G. M. Hodges, and L. J. Reames, 2012: A climatology and comparison of parameters for significant tornado events in the United States. *Wea. Forecasting*, **27**, 106–123, https://doi.org/10.1175/WAF-D-11-00008.1.

Guastini, C. T., and L. F. Bosart, 2016: Analysis of a progressive derecho climatology and associated formation environments. *Mon. Wea. Rev.*, **144**, 1363–1382, https://doi.org/10.1175/MWR-D-15-0256.1.

Guyer, J. L., and A. R. Dean, 2010: Tornadoes within weak CAPE environments across the continental United States. *25th Conf.*

on Severe Local Storms, Denver, CO, Amer. Meteor. Soc., 1.5, https://ams.confex.com/ams/pdfpapers/175725.pdf.

Hamill, T. M., R. S. Schneider, H. E. Brooks, G. S. Forbes, H. B. Bluestein, M. Steinberg, D. Meléndez, and R. M. Dole, 2005: The May 2003 extended tornado outbreak. *Bull. Amer. Meteor. Soc.*, **86**, 531–542, https://doi.org/10.1175/BAMS-86-4-531.

Hart, J. A., and W. Korotky, 1991: The SHARP workstation v1.50 users guide. National Weather Service, NOAA, U.S. Dept. of Commerce, 30 pp. [Available from NWS Eastern Region Headquarters, 630 Johnson Ave., Bohemia, NY 11716.]

Harvey, B. J., L. C. Shaffrey, and T. J. Woollings, 2014: Equator-to-pole temperature differences and the extra-tropical storm track responses of the CMIP5 climate models. *Climate Dyn.*, **43**, 1171–1182, https://doi.org/10.1007/s00382-013-1883-9.

Helfand, H. M., and S. D. Schubert, 1995: Climatology of the simulated Great Plains low-level jet and its contribution to the continental moisture budget of the United States. *J. Climate*, **8**, 784–806, https://doi.org/10.1175/1520-0442(1995)008<0784:COTSGP>2.0.CO;2.

Hersbach, H., and D. Dee, 2016: ERA5 reanalysis is in production. *ECMWF Newsletter*, No. 147, ECMWF, Reading, United Kingdom, 7, https://www.ecmwf.int/sites/default/files/elibrary/2016/16299-newsletter-no147-spring-2016.pdf.

Higgins, R. W., Y. Yao, E. S. Yarosh, J. E. Janowiak, and K. C. Mo, 1997: Influence of the Great Plains low-level jet on summertime precipitation and moisture transport over the central United States. *J. Climate*, **10**, 481–507, https://doi.org/10.1175/1520-0442(1997)010<0481:IOTGPL>2.0.CO;2.

Hoch, J., and P. Markowski, 2005: A climatology of springtime dryline position in the U.S. Great Plains region. *J. Climate*, **18**, 2132–2137, https://doi.org/10.1175/JCLI3392.1.

Holton, J. R., 1973: An introduction to dynamic meteorology. *Amer. J. Phys.*, **41**, 752–754, https://doi.org/10.1119/1.1987371.

Hoogewind, K. A., M. E. Baldwin, and R. J. Trapp, 2017: The impact of climate change on hazardous convective weather in the United States: Insight from high-resolution dynamical downscaling. *J. Climate*, **30**, 10 081–10 100, https://doi.org/10.1175/JCLI-D-16-0885.1.

Hunter, J. D., 2007: Matplotlib: A 2d graphics environment. *Comput. Sci. Eng.*, **9**, 90–95, https://doi.org/10.1109/MCSE.2007.55.

Johns, R. H., 1993: Meteorological conditions associated with bow echo development in convective storms. *Wea. Forecasting*, **8**, 294–299, https://doi.org/10.1175/1520-0434(1993)008<0294:MCAWBE>2.0.CO;2.

——, and C. A. Doswell III, 1992: Severe local storms forecasting. *Wea. Forecasting*, **7**, 588–612, https://doi.org/10.1175/1520-0434(1992)007<0588:SLSF>2.0.CO;2.

Jones, T. A., K. M. McGrath, and J. T. Snow, 2004: Association between NSSL mesocyclone detection algorithm-detected vortices and tornadoes. *Wea. Forecasting*, **19**, 872–890, https://doi.org/10.1175/1520-0434(2004)019<0872:ABNMDA>2.0.CO;2.

Kaspi, Y., and T. Schneider, 2013: The role of stationary eddies in shaping midlatitude storm tracks. *J. Atmos. Sci.*, **70**, 2596–2613, https://doi.org/10.1175/JAS-D-12-082.1.

Klein, S. A., X. Jiang, J. Boyle, S. Malyshev, and S. Xie, 2006: Diagnosis of the summertime warm and dry bias over the U.S. Southern Great Plains in the GFDL climate model using a weather forecasting approach. *Geophys. Res. Lett.*, **33**, L18805, https://doi.org/10.1029/2006GL027567.

Koster, R. D., and M. J. Suarez, 2001: Soil moisture memory in climate models. *J. Hydrometeor.*, **2**, 558–570, https://doi.org/10.1175/1525-7541(2001)002<0558:SMMICM>2.0.CO;2.

——, and Coauthors, 2004: Regions of strong coupling between soil moisture and precipitation. *Science*, **305**, 1138–1140, https://doi.org/10.1126/science.1100217.

Lanicci, J. M., and T. T. Warner, 1991a: A synoptic climatology of the elevated mixed-layer inversion over the southern Great Plains in spring. Part I: Structure, dynamics, and seasonal evolution. *Wea. Forecasting*, **6**, 181–197, https://doi.org/10.1175/1520-0434(1991)006<0181:ASCOTE>2.0.CO;2.

——, and ——, 1991b: A synoptic climatology of the elevated mixed-layer inversion over the southern Great Plains in spring. Part II: The life cycle of the lid. *Wea. Forecasting*, **6**, 198–213, https://doi.org/10.1175/1520-0434(1991)006<0198:ASCOTE>2.0.CO;2.

——, and ——, 1991c: A synoptic climatology of the elevated mixed-layer inversion over the southern Great Plains in spring. Part III: Relationship to severe-storms climatology. *Wea. Forecasting*, **6**, 214–226, https://doi.org/10.1175/1520-0434(1991)006<0214:ASCOTE>2.0.CO;2.

Lin, Y., W. Dong, M. Zhang, Y. Xie, W. Xue, J. Huang, and Y. Luo, 2017: Causes of model dry and warm bias over central US and impact on climate projections. *Nat. Commun.*, **8**, 881, https://doi.org/10.1038/s41467-017-01040-2.

Ludlam, F., 1963: Severe local storms: A review. *Severe Local Storms, Meteor. Monogr.*, Vol. 5, Amer. Meteor. Soc., 1–32, https://doi.org/10.1007/978-1-940033-56-3_.

Mercer, A. E., M. B. Richman, C. A. Doswell III, C. M. Shafer, and L. M. Leslie, 2012: Synoptic composites of tornadic and non-tornadic outbreaks. *Mon. Wea. Rev.*, **140**, 2590–2608, https://doi.org/10.1175/MWR-D-12-00029.1.

Miller, P. W., and T. L. Mote, 2017: A climatology of weakly forced and pulse thunderstorms in the southeast United States. *J. Appl. Meteor. Climatol.*, **56**, 3017–3033, https://doi.org/10.1175/JAMC-D-17-0005.1.

Mo, K. C., and H.-M. H. Juang, 2003: Relationships between soil moisture and summer precipitation over the Great Plains and the southwest. *J. Geophys. Res.*, **108**, 8610, https://doi.org/10.1029/2002JD002952.

Mueller, B., and S. I. Seneviratne, 2014: Systematic land climate and evapotranspiration biases in CMIP5 simulations. *Geophys. Res. Lett.*, **41**, 128–134, https://doi.org/10.1002/2013GL058055.

Neale, R. B., and Coauthors, 2012: Description of the NCAR Community Atmosphere Model (CAM 5.0). NCAR Tech. Note NCAR/TN-486+STR, 274 pp., www.cesm.ucar.edu/models/cesm1.0/cam/docs/description/cam5_desc.pdf.

Nesbitt, S. W., and E. J. Zipser, 2003: The diurnal cycle of rainfall and convective intensity according to three years of TRMM measurements. *J. Climate*, **16**, 1456–1475, https://doi.org/10.1175/1520-0442-16.10.1456.

Parker, W. S., 2016: Reanalyses and observations: What's the difference? *Bull. Amer. Meteor. Soc.*, **97**, 1565–1572, https://doi.org/10.1175/BAMS-D-14-00226.1.

Phillips, T. J., and S. A. Klein, 2014: Land-atmosphere coupling manifested in warm-season observations on the U.S. Southern Great Plains. *J. Geophys. Res. Atmos.*, **119**, 509–528, https://doi.org/10.1002/2013JD020492.

Rasmussen, E. N., 2003: Refined supercell and tornado forecast parameters. *Wea. Forecasting*, **18**, 530–535, https://doi.org/10.1175/1520-0434(2003)18<530:RSATFP>2.0.CO;2.

——, and D. O. Blanchard, 1998: A baseline climatology of sounding-derived supercell and tornado forecast parameters. *Wea. Forecasting*, **13**, 1148–1164, https://doi.org/10.1175/1520-0434(1998)013<1148:ABCOSD>2.0.CO;2.

Reitan, C. H., 1974: Frequencies of cyclones and cyclogenesis for North America, 1951–1970. *Mon. Wea. Rev.*, **102**,

861–868, https://doi.org/10.1175/1520-0493(1974)102<0861:FOCACF>2.0.CO;2.

Rhea, J. O., 1966: A study of thunderstorm formation along dry lines. *J. Appl. Meteor.*, **5**, 58–63, https://doi.org/10.1175/1520-0450(1966)005<0058:ASOTFA>2.0.CO;2.

Ribeiro, B. Z., and L. F. Bosart, 2018: Elevated mixed layers and associated severe thunderstorm environments in South and North Americas. *Mon. Wea. Rev.*, **146**, 3–28, https://doi.org/10.1175/MWR-D-17-0121.1.

Rieck, J. K., C. W. Böning, R. J. Greatbatch, and M. Scheinert, 2015: Seasonal variability of eddy kinetic energy in a global high-resolution ocean model. *Geophys. Res. Lett.*, **42**, 9379–9386, https://doi.org/10.1002/2015GL066152.

Robinson, E. D., R. J. Trapp, and M. E. Baldwin, 2013: The geospatial and temporal distributions of severe thunderstorms from high-resolution dynamical downscaling. *J. Appl. Meteor. Climatol.*, **52**, 2147–2161, https://doi.org/10.1175/JAMC-D-12-0131.1.

Romps, D. M., J. T. Seeley, D. Vollaro, and J. Molinari, 2014: Projected increase in lightning strikes in the United States due to global warming. *Science*, **346**, 851–854, https://doi.org/10.1126/science.1259100.

Rotunno, R., and J. B. Klemp, 1982: The influence of the shear-induced pressure gradient on thunderstorm motion. *Mon. Wea. Rev.*, **110**, 136–151, https://doi.org/10.1175/1520-0493(1982)110<0136:TIOTSI>2.0.CO;2.

——, and ——, 1985: On the rotation and propagation of simulated supercell thunderstorms. *J. Atmos. Sci.*, **42**, 271–292, https://doi.org/10.1175/1520-0469(1985)042<0271:OTRAPO>2.0.CO;2.

——, and M. L. Weisman, 2003: Comment on "Linear and nonlinear propagation of supercell storms." *J. Atmos. Sci.*, **60**, 2413–2419, https://doi.org/10.1175/1520-0469(2003)060<2413:COLANP>2.0.CO;2.

Russell, D. R., 2006: Development of a time-domain, variable-period surface-wave magnitude measurement procedure for application at regional and teleseismic distances, Part I: Theory. *Bull. Seismol. Soc. Amer.*, **96**, 665–677, https://doi.org/10.1785/0120050055.

Schaefer, J. T., 1974: The life cycle of the dryline. *J. Appl. Meteor.*, **13**, 444–449, https://doi.org/10.1175/1520-0450(1974)013<0444:TLCOTD>2.0.CO;2.

——, and C. A. Doswell III, 1984: Empirical orthogonal function expansion applied to progressive tornado outbreaks. *J. Meteor. Soc. Japan*, **62**, 929–936, https://doi.org/10.2151/jmsj1965.62.6_929.

Schemm, S., and T. Schneider, 2018: Eddy lifetime, number, and diffusivity and the suppression of eddy kinetic energy in midwinter. *J. Climate*, **31**, 5649–5665, https://doi.org/10.1175/JCLI-D-17-0644.1.

Schultz, D. M., C. C. Weiss, and P. M. Hoffman, 2007: The synoptic regulation of dryline intensity. *Mon. Wea. Rev.*, **135**, 1699–1709, https://doi.org/10.1175/MWR3376.1.

Seeley, J. T., and D. M. Romps, 2015: The effect of global warming on severe thunderstorms in the United States. *J. Climate*, **28**, 2443–2458, https://doi.org/10.1175/JCLI-D-14-00382.1.

Sherburn, K. D., and M. D. Parker, 2014: Climatology and ingredients of significant severe convection in high-shear, low-CAPE environments. *Wea. Forecasting*, **29**, 854–877, https://doi.org/10.1175/WAF-D-13-00041.1.

——, ——, J. R. King, and G. M. Lackmann, 2016: Composite environments of severe and nonsevere high-shear, low-CAPE convective events. *Wea. Forecasting*, **31**, 1899–1927, https://doi.org/10.1175/WAF-D-16-0086.1.

Sheridan, S. C., and C. C. Lee, 2011: The self-organizing map in synoptic climatological research. *Prog. Phys. Geogr.*, **35**, 109–119, https://doi.org/10.1177/0309133310397582.

Singh, M. S., Z. Kuang, E. D. Maloney, W. M. Hannah, and B. O. Wolding, 2017: Increasing potential for intense tropical and subtropical thunderstorms under global warming. *Proc. Natl. Acad. Sci. USA*, **114**, 11 657–11 662, https://doi.org/10.1073/pnas.1707603114.

Stahle, D. W., and M. K. Cleaveland, 1992: Reconstruction and analysis of spring rainfall over the southeastern U.S. for the past 1000 years. *Bull. Amer. Meteor. Soc.*, **73**, 1947–1961, https://doi.org/10.1175/1520-0477(1992)073<1947:RAAOSR>2.0.CO;2.

Tamarin, T., and Y. Kaspi, 2016: The poleward motion of extratropical cyclones from a potential vorticity tendency analysis. *J. Atmos. Sci.*, **73**, 1687–1707, https://doi.org/10.1175/JAS-D-15-0168.1.

Tang, B. H., V. A. Gensini, and C. R. Homeyer, 2019: Trends in United States large hail environments and observations. *npj Climate Atmos. Sci.*, **2**, 45, https://doi.org/10.1038/s41612-019-0103-7.

Taszarek, M., H. E. Brooks, B. Czernecki, P. Szuster, and K. Fortuniak, 2018: Climatological aspects of convective parameters over Europe: A comparison of ERA-Interim and sounding data. *J. Climate*, **31**, 4281–4308, https://doi.org/10.1175/JCLI-D-17-0596.1.

Thompson, R. L., R. Edwards, J. A. Hart, K. L. Elmore, and P. Markowski, 2003: Close proximity soundings within supercell environments obtained from the Rapid Update Cycle. *Wea. Forecasting*, **18**, 1243–1261, https://doi.org/10.1175/1520-0434(2003)018<1243:CPSWSE>2.0.CO;2.

Tian, B., I. M. Held, N. C. Lau, and B. J. Soden, 2005: Diurnal cycle of summertime deep convection over North America: A satellite perspective. *J. Geophys. Res.*, **110**, D08108, https://doi.org/10.1029/2004JD005275.

Tippett, M. K., J. T. Allen, V. A. Gensini, and H. E. Brooks, 2015: Climate and hazardous convective weather. *Curr. Climate Change Rep.*, **1**, 60–73, https://doi.org/10.1007/s40641-015-0006-6.

——, C. Lepore, and J. E. Cohen, 2016: More tornadoes in the most extreme U.S. tornado outbreaks. *Science*, **354**, 1419–1423, https://doi.org/10.1126/science.aah7393.

Tochimoto, E., and H. Niino, 2016: Structural and environmental characteristics of extratropical cyclones that cause tornado outbreaks in the warm sector: A composite study. *Mon. Wea. Rev.*, **144**, 945–969, https://doi.org/10.1175/MWR-D-15-0015.1.

Trapp, R. J., N. S. Diffenbaugh, H. E. Brooks, M. E. Baldwin, E. D. Robinson, and J. S. Pal, 2007: Changes in severe thunderstorm environment frequency during the 21st century caused by anthropogenically enhanced global radiative forcing. *Proc. Natl. Acad. Sci. USA*, **104**, 19 719–19 723, https://doi.org/10.1073/pnas.0705494104.

——, ——, and A. Gluhovsky, 2009: Transient response of severe thunderstorm forcing to elevated greenhouse gas concentrations. *Geophys. Res. Lett.*, **36**, L01703, https://doi.org/10.1029/2008GL036203.

——, E. D. Robinson, M. E. Baldwin, N. S. Diffenbaugh, and B. R. Schwedler, 2011: Regional climate of hazardous convective weather through high-resolution dynamical downscaling. *Climate Dyn.*, **37**, 677–688, https://doi.org/10.1007/s00382-010-0826-y.

Ulbrich, U., J. G. Pinto, H. Kupfer, G. C. Leckebusch, T. Spangehl, and M. Reyers, 2008: Changing Northern Hemisphere storm

tracks in an ensemble of IPCC climate change simulations. *J. Climate*, **21**, 1669–1679, https://doi.org/10.1175/2007JCLI1992.1.

Ullrich, P. A., and C. M. Zarzycki, 2017: Tempestextremes: A framework for scale-insensitive pointwise feature tracking on unstructured grids. *Geosci. Model Dev.*, **10**, 1069–1090, https://doi.org/10.5194/gmd-10-1069-2017.

Wagner, T. J., W. F. Feltz, and S. A. Ackerman, 2008: The temporal evolution of convective indices in storm-producing environments. *Wea. Forecasting*, **23**, 786–794, https://doi.org/10.1175/2008WAF2007046.1.

Wallace, J. M., 1975: Diurnal variations in precipitation and thunderstorm frequency over the conterminous United States. *Mon. Wea. Rev.*, **103**, 406–419, https://doi.org/10.1175/1520-0493(1975)103<0406:DVIPAT>2.0.CO;2.

Walters, C. K., J. A. Winkler, R. P. Shadbolt, J. van Ravensway, and G. D. Bierly, 2008: A long-term climatology of southerly and northerly low-level jets for the central United States. *Ann. Assoc. Amer. Geogr.*, **98**, 521–552, https://doi.org/10.1080/00045600802046387.

——, ——, S. Husseini, R. Keeling, J. Nikolic, and S. Zhong, 2014: Low-level jets in the North American Regional Reanalysis (NARR): A comparison with rawinsonde observations. *J. Appl. Meteor. Climatol.*, **53**, 2093–2113, https://doi.org/10.1175/JAMC-D-13-0364.1.

Weaver, S. J., and S. Nigam, 2008: Variability of the Great Plains low-level jet: Large-scale circulation context and hydroclimate impacts. *J. Climate*, **21**, 1532–1551, https://doi.org/10.1175/2007JCLI1586.1.

——, S. Baxter, and A. Kumar, 2012: Climatic role of North American low-level jets on U.S. regional tornado activity. *J. Climate*, **25**, 6666–6683, https://doi.org/10.1175/JCLI-D-11-00568.1.

Weisman, M. L., and R. Rotunno, 2000: The use of vertical wind shear versus helicity in interpreting supercell dynamics. *J. Atmos. Sci.*, **57**, 1452–1472, https://doi.org/10.1175/1520-0469(2000)057<1452:TUOVWS>2.0.CO;2.

Whiteman, C. D., X. Bian, and S. Zhong, 1997: Low-level jet climatology from enhanced rawinsonde observations at a site in the southern Great Plains. *J. Appl. Meteor.*, **36**, 1363–1376, https://doi.org/10.1175/1520-0450(1997)036<1363:LLJCFE>2.0.CO;2.

Williams, E., and N. Renno, 1993: An analysis of the conditional instability of the tropical atmosphere. *Mon. Wea. Rev.*, **121**, 21–36, https://doi.org/10.1175/1520-0493(1993)121<0021:AAOTCI>2.0.CO;2.

Xue, M., and W. J. Martin, 2006: A high-resolution modeling study of the 24 May 2002 dryline case during IHOP. Part I: Numerical simulation and general evolution of the dryline and convection. *Mon. Wea. Rev.*, **134**, 149–171, https://doi.org/10.1175/MWR3071.1.

Yin, J. H., 2005: A consistent poleward shift of the storm tracks in simulations of 21st century climate. *Geophys. Res. Lett.*, **32**, L18701, https://doi.org/10.1029/2005GL023684.

Zarzycki, C., 2018: Projecting changes in societally impactful northeastern U.S. snowstorms. *Geophys. Res. Lett.*, **45**, 12 067–12 075, https://doi.org/10.1029/2018GL079820.

Zhang, G. J., and N. A. McFarlane, 1995: Sensitivity of climate simulations to the parameterization of cumulus convection in the Canadian Climate Centre general circulation model. *Atmos.–Ocean*, **33**, 407–446, https://doi.org/10.1080/07055900.1995.9649539.

Ziegler, C. L., and C. E. Hane, 1993: An observational study of the dryline. *Mon. Wea. Rev.*, **121**, 1134–1151, https://doi.org/10.1175/1520-0493(1993)121<1134:AOSOTD>2.0.CO;2.

——, and E. N. Rasmussen, 1998: The initiation of moist convection at the dryline: Forecasting issues from a case study perspective. *Wea. Forecasting*, **13**, 1106–1131, https://doi.org/10.1175/1520-0434(1998)013<1106:TIOMCA>2.0.CO;2.

Zishka, K. M., and P. J. Smith, 1980: The climatology of cyclones and anticyclones over North America and surrounding ocean environs for January and July, 1950–77. *Mon. Wea. Rev.*, **108**, 387–401, https://doi.org/10.1175/1520-0493(1980)108<0387:TCOCAA>2.0.CO;2.